iScience

CellPress

Article

Giant Electroresistance in Ferroionic Tunnel Junctions

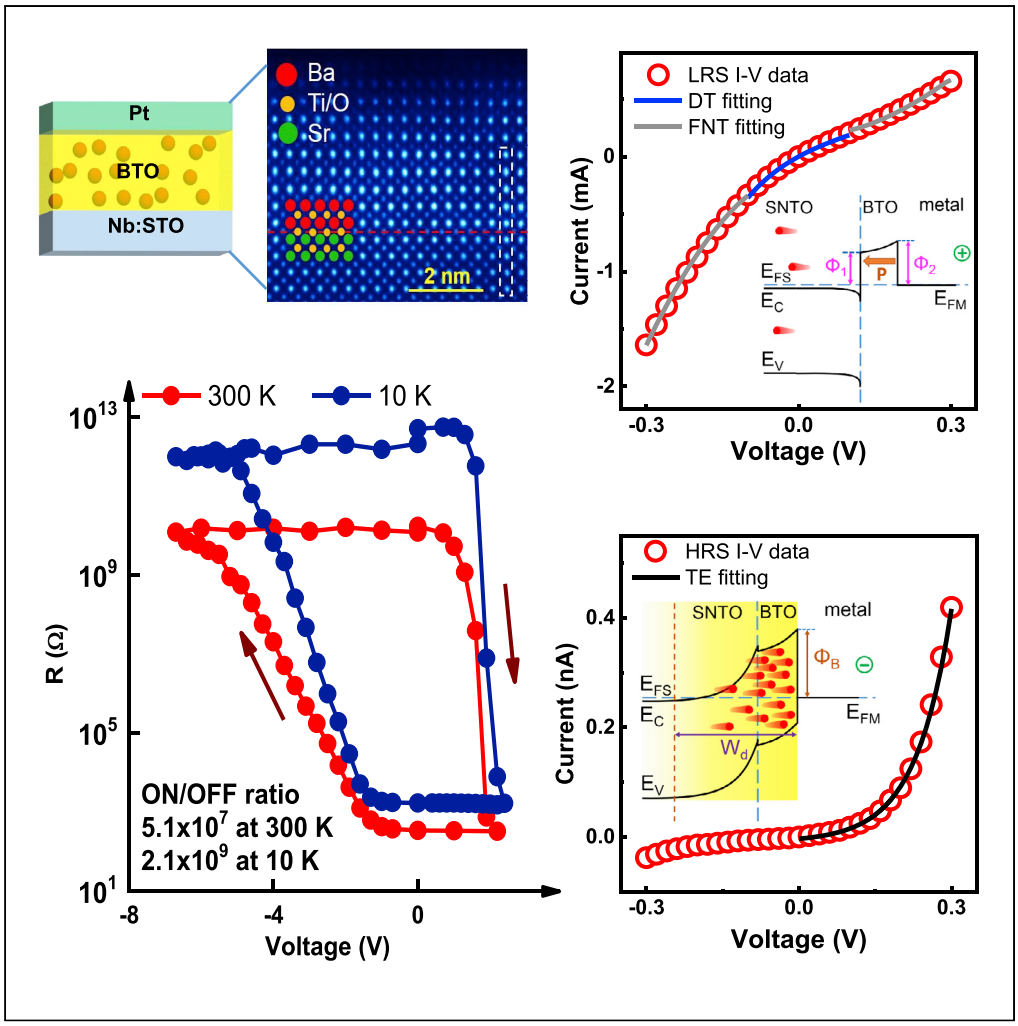

Jiankun Li, Ning Li, Chen Ge, ..., Can Wang, Guozhen Yang, Kuijuan Jin

gechen@iphy.ac.cn (C.G.)
p-gao@pku.edu.cn (P.G.)
kjjin@iphy.ac.cn (K.J.)

HIGHLIGHTS

Ferroionic tunnel junctions with ON/OFF ratio of 5.1×10^7 at 300 K were demonstrated

Both ferroelectric and ionic degrees of freedom were exploited in the device

Field-induced oxygen vacancy migration switches it between FTJ and Schottky junction

Li et al., iScience 16, 368–377
June 28, 2019
https://doi.org/10.1016/j.isci.2019.05.043

iScience

CellPress

Article

Giant Electroresistance in Ferroionic Tunnel Junctions

Jiankun Li,[1,6] Ning Li,[2,6] Chen Ge,[1,3,7,*] Heyi Huang,[1] Yuanwei Sun,[2] Peng Gao,[2,4,*] Meng He,[1] Can Wang,[1,5] Guozhen Yang,[1] and Kuijuan Jin[1,5,*]

SUMMARY

Oxide-based resistive switching devices, including ferroelectric tunnel junctions and resistance random access memory, are promising candidates for the next-generation non-volatile memory technology. In this work, we propose a ferroionic tunnel junction to realize a giant electroresistance. It functions as a ferroelectric tunnel junction at low resistance state and as a Schottky junction at high resistance state, due to interface engineering through the field-induced migration of oxygen vacancies. An extremely large electroresistance with ON/OFF ratios of 5.1×10^7 at room temperature and 2.1×10^9 at 10 K is achieved, using an ultrathin $BaTiO_{3-\delta}$ layer as the ferroelectric barrier and a semiconducting Nb-doped $SrTiO_3$ substrate as the bottom electrode. The results point toward an appealing way for the design of high-performance resistive switching devices based on ultrathin oxide heterostructures by ionic controlled interface engineering.

INTRODUCTION

Nanoscale ferroelectric systems are a realm of fascination in condensed-matter physics and material community (Yang et al., 2017; Duan et al., 2006). Ferroelectric tunnel junction (FTJ), an ultrathin ferroelectric layer sandwiched by two metallic electrodes (Qin et al., 2016; Li et al., 2015; Pantel et al., 2012), attracts extensive interests as one of the promising ways to achieve semiconductor memories for its advantages of non-destructive readout (Garcia and Bibes, 2014; Scott, 2007; Li et al., 2017a; Garcia et al., 2009), high switching speed (Garcia and Bibes, 2014; Chanthbouala et al., 2012; Yoon et al., 2017), high endurance (Boyn et al., 2017), and simple structure (Guo et al., 2017; Yau et al., 2017). The basic concept of FTJs (called a polar switch at that time) was first proposed by Esaki et al. (1971). The idea is to control the tunnel transmission by ferroelectric polarization modulated barriers, which leads to tunnel electroresistance (Tsymbal and Kohlstedt, 2006; Zhuravlev et al., 2005). The ON/OFF ratio, which is defined as the ratio of the high resistance to the low resistance, is one of the most important parameters to characterize these devices because a higher ON/OFF ratio can help to act as a promising candidate for low-power and high-performance electronic devices (Linn et al., 2010). In 2003, Contreras et al. found two well-defined stable and reproducible resistance states in $Pt/Pb(Zr_{0.52}Ti_{0.48})O_3/SrRuO_3$ junctions with an ON/OFF ratio close to four and confirmed that the polarization reversal in the ferroelectric barrier is the origin of the resistance switching (Rodríguez Contreras et al., 2003). Since then, endeavors of improving the ON/OFF ratio have been made from 10 to 10^3 in devices consisting of two metal electrodes separated by a nanometer-thick ferroelectric barrier (Zenkevich et al., 2013; Yin et al., 2013; Soni et al., 2014; Li et al., 2014). Furthermore, Wen et al. enhanced the ON/OFF ratios to 10^4–10^6 in metal/ferroelectric/semiconductor (MFS) structures by utilizing an extra space charge layer at the ferroelectric/semiconductor interface in recent years, which greatly promoted the development of FTJs (Wen et al., 2013; Xi et al., 2017). In addition, Guo et al. achieved a giant ON/OFF ratio in MFS structures through interface engineering, indicating the potential of MFS structures (Guo et al., 2018).

In FTJs, as the thickness of ferroelectric layer reduces to a few nanometers, quantum-mechanical tunneling commonly dominates the electronic conduction: direct tunneling (DT) is conspicuous at a low voltage, whereas Fowler-Nordheim tunneling (FNT) plays a key role at a high voltage (Garcia and Bibes, 2014; Pantel and Alexe, 2010). The imperfect screening of ferroelectric polarization charges at the interface leads to different average barrier heights depending on the polarization direction, which gives rise to the high resistance state (HRS) and low resistance state (LRS) (Zhuravlev et al., 2005). Comparing with tunneling current, the current induced by thermionic emission (TE) mechanism is usually negligible because of its low value. As the barrier width increases, the tunneling current decreases exponentially and the TE current dominates. Moreover, the TE current can also be suppressed by raising the barrier height. Therefore, an extremely high

[1]Beijing National Laboratory for Condensed Matter Physics, Institute of Physics, Chinese Academy of Sciences, Beijing 100190, China

[2]International Center for Quantum Materials and Electron Microscopy Laboratory, School of Physics, Peking University, Beijing 100871, China

[3]Key Laboratory of Polar Materials and Devices, Ministry of Education, Shanghai 200241, China

[4]Collaborative Innovation Centre of Quantum Matter, Beijing 100871, China

[5]Songshan Lake Materials Laboratory, Dongguan, Guangdong 523808, China

[6]These authors contributed equally

[7]Lead Contact

*Correspondence: gechen@iphy.ac.cn (C.G.), p-gao@pku.edu.cn (P.G.), kjjin@iphy.ac.cn (K.J.)

https://doi.org/10.1016/j.isci.2019.05.043

ON/OFF ratio can be anticipated by harnessing the DT-induced LRS and TE-induced HRS in FTJ devices. The main challenge is to effectively manipulate the conduction mechanism accompanying the polarization reversal.

The voltage-driven ion migration offers a promising way toward the achievement of this goal. Oxygen vacancies ($V_O^{\cdot\cdot}$) are commonly regarded as important functional defects in oxides (Li et al., 2017b; Jang et al., 2017; Adepalli et al., 2017; Lu et al., 2017; Christensen et al., 2017; Yao et al., 2014) and generally function as mobile electron donors (Ge et al., 2015). It is well known that the voltage-driven migration of positively charged $V_O^{\cdot\cdot}$ is responsible for resistive switching phenomena in complex oxide films (Waser et al., 2009; Cooper et al., 2017; Yao et al., 2017; Hu et al., 2016). For FTJs, the electric field could be extremely strong owing to its operation on the nanoscale ferroelectric film, even though only a few volts are applied on the barriers. This strong electric field further facilitates the movement of $V_O^{\cdot\cdot}$ across the nanoscale ferroelectric films (Yang et al., 2017). Recently, several pioneering works have been performed to investigate the role of oxygen vacancies in FTJ devices (Qin et al., 2016; Lu et al., 2017). Hu et al. realized a large ON/OFF ratio of 10^5 in a 3-nm-thick $Sm_{0.1}Bi_{0.9}FeO_3$-based FTJ device, where large tunneling electroresistance originates from the transition between DT and Schottky TE induced by oxygen vacancy migration (Hu et al., 2016). Furthermore, oxide materials usually possess a wide range of band structures depending on the band filling controlled by the $V_O^{\cdot\cdot}$ concentration. A high concentration of $V_O^{\cdot\cdot}$ can change the material property and even promote emergent functional phenomena (Das et al., 2017). Thus, the possibility to dynamically manipulate $V_O^{\cdot\cdot}$ in FTJs provides an opportunity to discover novel physical phenomena. In this work, we aim to obtain a large DT current at LRS and achieve a low TE current at HRS by modifying the oxide barrier via ionic degree of freedom.

Herein, we achieve a giant electroresistance effect with an extremely high ON/OFF ratio in ferroionic tunnel junction (FITJ). It works between FTJ and Schottky junction by switching mobile functional ions. A giant electroresistance, with ON/OFF ratios as high as 5.1×10^7 at room temperature and 2.1×10^9 at 10 K, has been achieved through controlling the concentration of $V_O^{\cdot\cdot}$ and the kind of metallic electrodes. The result raises the prospect of concurrently exploiting the ferroelectric and ionic degrees of freedom for new generations of nanoscale perovskite-based devices.

RESULTS

Properties of Ultrathin BTO Films with Different Oxygen Vacancy Concentrations

We choose an MFS structure to investigate FITJs due to its advantages from the space charge layer in semiconductors (Xi et al., 2017; Asa and Bertacco, 2018). Epitaxial BTO ultrathin films are grown on single-crystalline 0.7 wt% Nb-doped $SrTiO_3$ (SNTO) substrates through pulsed laser deposition technique. The details about the film growth procedure can be found in Transparent Methods. The SNTO substrate acts as the semiconductor layer, and Pt is chosen as the metal layer because it has a large work function (5.65 eV) to induce a high barrier. Non-ferroelectric $SrTiO_3$ (STO) films, fabricated under the same conditions with BTO films, are also studied for comparison because non-ferroelectric STO has a band structure very similar to that of ferroelectric BTO and provide an excellent control sample to study the ionic modulation phenomena (Christensen et al., 2017; Zhang et al., 2011; Peacock and Robertson, 2002).

A variety of deposition oxygen pressures are used to optimize the effect of $V_O^{\cdot\cdot}$. Figure 1 shows the basic properties of BTO/SNTO heterostructure with 7 u.c. thick BTO film deposited under an oxygen pressure of 0.01 Pa. From the high-angle annular dark field (HAADF) image of scanning transmission electron microscopy (STEM), we can see a sharp interface between BTO and SNTO, indicating a good epitaxy quality (Figure 1A). Atomic force microscopy (AFM) measurement with a scanned area of $6 \times 6\ \mu m^2$ shows that the epitaxial film was atomically flat with terrace structure (Figures 1B and 1C). The high quality of epitaxial films, which prevents short circuits between top and bottom electrodes, is crucial for the sequent fabrication of junction devices.

Before measuring the electrical properties of the devices, we first characterize the ferroelectricity of the bare BTO films with thickness of 7 u.c. through piezoresponse force microscopy (PFM) technique. Figure 1D shows the out-of-plane PFM phase image of antiparallel domains written with ± 9.5 V on BTO(0.01) surface. Here, we use BTO(O_p) (STO(O_p)) notation to denote the BTO (STO) ultrathin films fabricated under O_p Pa oxygen pressure for the convenience of expression. A clear phase contrast of $\sim 180^\circ$ was observed in the BTO(0.01) (Figure 1D), BTO(1) and BTO(20) (Figure S1). Interestingly, we can obtain a clear PFM phase

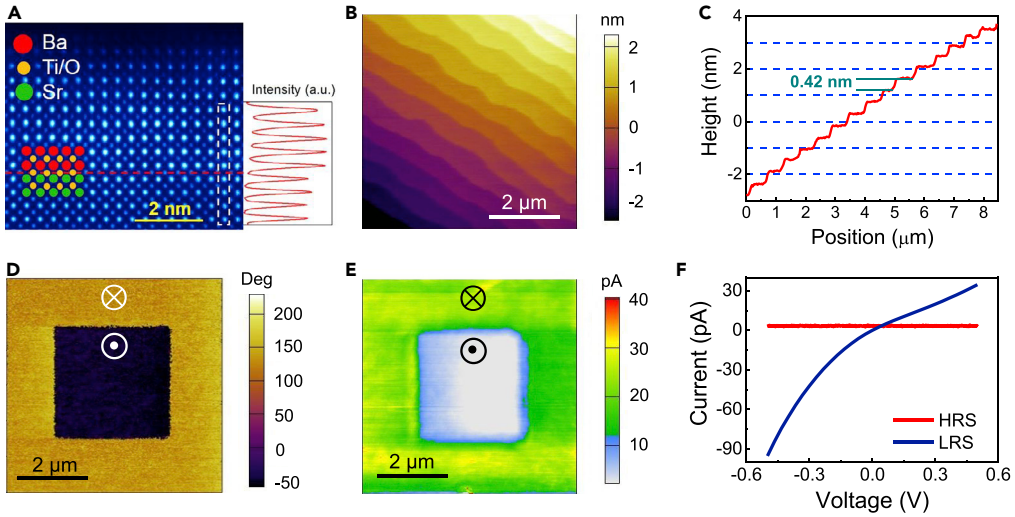

Figure 1. Geometry and Ferroelectric Properties of 7 u.c.-Thick $BaTiO_3$ (BTO) Film Deposited on Nb-doped $SrTiO_3$ (SNTO) Substrate

The BTO/SNTO heterostructure is fabricated under 0.01 Pa oxygen pressure.

(A) A cross-sectional high-angle annular dark field (HAADF) image. The red, orange, and green circles display the Ba, Ti/O, and Sr sites, respectively. The interface is marked by the red line. The intensity profile, with respect to the white maker, determines the position of interface.

(B) Atomic force microscopy (AFM) surface morphology of the heterostructure. The film displays atomically flat surface and uniform terraces.

(C) Height profile of the region marked by the red line in (B).

(D) Out-of-plane piezoresponse force microscopy (PFM) phase contrast image. The pattern was written by scanning the conductive-tip bias with ±9.5 V.

(E) Tunneling current mapping acquired by conductive AFM (C-AFM) after the domain patterning and performed by scanning a 0.5-V biased conductive-tip over the two domains.

(F) Current-voltage (*I-V*) curves at low resistance state (LRS) and high resistance state (HRS) measured by the C-AFM tip.

and amplitude contrast in the STO(0.01) film (Figure S1), which is mainly ascribed to the surface electrochemical behavior from ionic movements (Yang et al., 2017). The phase contrast becomes weaker with increasing deposition oxygen pressure in STO films (Figure S1). The V_{AC}-dependent PFM measurements further imply coupled ferroelectric-electrochemical (ferroionic) states in the BTO ultrathin films deposited under low oxygen pressures (Figure S2) (Balke et al., 2015).

We also performed the local current mapping measurement using conductive AFM (C-AFM). A clear current contrast between two written domains implies that the ferroionic state modifies the local conduction of BTO(0.01) through the applied bias (Figure 1E). There is a larger current for the downward domain than for the upward domain, consistent with the previous studies (Wen et al., 2013; Xi et al., 2017; Hu et al., 2016). The local current-voltage (*I-V*) curves at LRS and HRS measured by the C-AFM tip shows a typical resistive switching phenomenon (Figure 1F).

Room-Temperature Electroresistance in BTO- and STO-Based Devices

Now we turn to investigate the electrical properties of tunnel junctions with the BTO and STO ultrathin films. The microscale Pt electrodes were patterned on the film surfaces via the standard photolithography method. Here, a thickness of 7 u.c. was chosen according to our investigation on the thickness dependence of device performance (Figure S3). The pristine ferroelectric polarization state of the BTO layers is pointing to the top electrode. All Pt/BTO/SNTO and Pt/STO/SNTO devices exhibit non-volatile resistance switching behavior, as shown in resistance-voltage (*R-V*) hysteresis loops (Figure S4). Figure 2A shows the largest *R-V* hysteresis loops measured in the Pt/BTO(0.01)/SNTO device at room temperature. Positive bias sets the device to LRS, whereas negative bias switches the device to HRS, in agreement with the C-AFM measurements. The resistances at HRS and LRS of BTO- and STO-based tunnel junctions and corresponding ON/OFF ratios are summarized in Figures 2B and S5, respectively. It can be seen that the HRS of

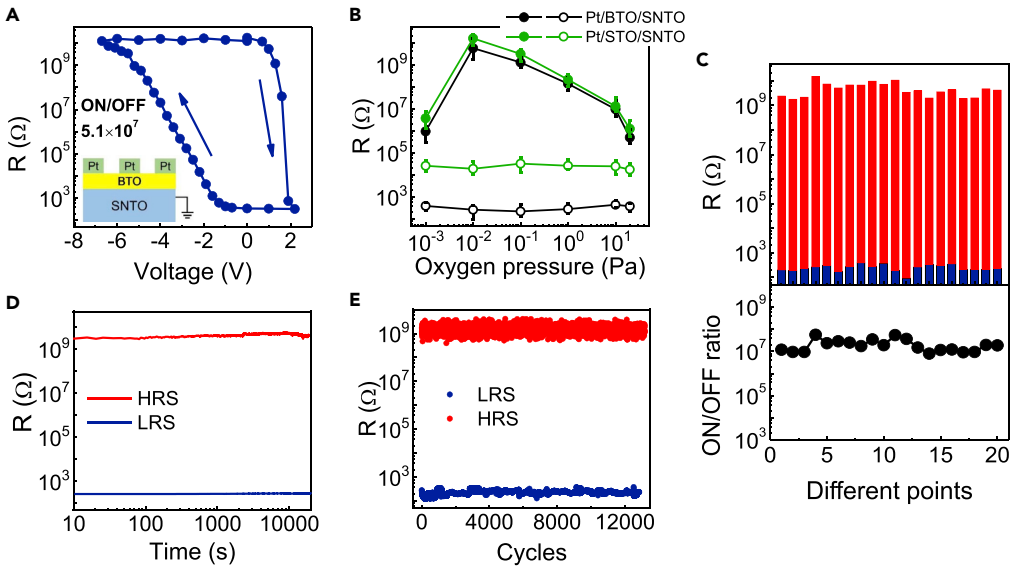

Figure 2. Device Performance of the Pt/BTO/SNTO Heterostructures

(A) A typical resistance memory loop as a function of write voltage at room temperature. The arrows indicate the direction of the applied pulse sequence, and the read voltage is 0.1 V. The inset indicates the schematic description of the devices.

(B) HRS and LRS resistances of BTO- and STO-based devices as a function of deposited oxygen pressure at room temperature. The resistances of LRS for both BTO and STO devices prepared under different oxygen pressures were obtained under the same write voltage of +2.2 V. At HRS, the resistances were obtained using the write voltage slightly lower than the breakdown voltage. The HRS and LRS resistances are represented by solid symbols and open symbols, respectively. The vertical error bars correspond to deviations of resistance from 10 devices.

(C) "ON" (dark blue) and "OFF" (red) resistance states of 20 different memory cells (upper panel) and the corresponding ON/OFF ratios (lower panel).

(D) Retention property up to more than 10^4 s. The pulse width is about 200 ms.

(E) Fatigue property for more than 12,000 cycles. In each cycle, the writing voltages are −7 V for HRS and +2.2 V for LRS.

STO-based devices is slightly higher than that of BTO-based devices (Figure 2B). This result confirms the dominant role of the oxygen vacancy accumulation for the HRS in our devices. The resistance of HRS becomes larger with the decrease of the oxygen pressure, except for the device fabricated under the lowest oxygen pressure. From the atom contrast in the HAADF image of Pt/BTO(0.001)/SNTO device (Figure S6), there exists a large structural distortion in the samples grown under 0.001 Pa due to a large amount of oxygen vacancies. We believe that this large structural distortion could be responsible for this reduced HRS. The oxygen vacancy concentration decreases as the deposited oxygen pressure increases. At HRS driven by negative biases, less $V_O^{\cdot\cdot}$ accumulates to decrease the height and width of the Schottky barrier at the Pt/BTO interface with increasing the oxygen pressure. Therefore, the maximum resistance emerges in BTO(0.01). In contrast, LRS resistances show no dependence on the oxygen pressure. LRS resistances in BTO- and STO-based devices remain 10^2 and 10^4 ohms with the variation of deposited oxygen pressure, respectively (Figure 2B). Owing to a lower LRS resistance, ON/OFF ratios in BTO-based devices are always higher than those in STO-based devices, demonstrating the role of ferroelectricity. The atomic displacements of Ti atoms were carefully analyzed in the HAADF image of BTO(0.01), confirming the existence of ferroelectricity (Figure S7). A giant ON/OFF ratio of 5.1×10^7 is obtained in the BTO(0.01) device at room temperature. To further confirm the role of $V_O^{\cdot\cdot}$ in increasing the ON/OFF ratio, BTO(0.01) film was annealed in oxygen atmosphere at 573 K for 30 min and then Au top electrodes were prepared and patterned. The ON/OFF ratio of the Au/annealed BTO(0.01)/SNTO device reduced four orders of magnitude compared with the unannealed device (Figure S8).

Figure 2C shows the HRS and LRS resistances reading at +0.1 V for various Pt/BTO(0.01)/SNTO devices, suggesting good uniformity and reproducibility. The other BTO-based devices also exhibit good uniformity (Figure S9). Moreover, we performed the retention tests of BTO-based devices (Figures 2D and S10). HRS and LRS keep almost constant during 10^4 s, suggesting an excellent nonvolatility. Figure 2E

shows fatigue tests of the resistance switching effect under bipolar pulse cycling of the Pt/BTO(0.01)/SNTO device. The write pulses of +2.2 and −7 V were applied alternately on the Pt top electrode. The repetitive bistable resistance state with ON/OFF ratio of $\sim 10^7$ could be maintained during up to 10^4 cycles, showing good switching property.

Furthermore, BTO devices with various top electrodes (Au, Cr, and Ti) were fabricated to enable us to get more insights into the effects of the top electrodes on the ferroionic electroresistance. The *R-V* characteristics of BTO films deposited under various oxygen pressures with different top electrode materials are shown in Figure 3. Similar to the devices with Pt top electrodes, the resistance of LRS is in the same range of about a few hundred ohms and the HRS resistance increases with the decreasing oxygen pressure, reaching a maximum at 0.01 Pa (Figure S11). Higher resistance of HRS can be achieved with a higher work function of the top metals (Ti 4.33 eV, Cr 4.5 eV, Au 5.1 eV, Pt 5.6 eV). Correspondingly, the ON/OFF ratio increases with the increase of work function and reaches a maximum in the Pt/BTO(0.01)/SNTO device (Figure S12). This result implies the important role of the metal/barrier interface.

Temperature-Dependent Electroresistance in Pt/BTO/SNTO Devices

Figure 4A represents the temperature-dependent LRS and HRS resistances of the BTO-based devices deposited under various oxygen pressures. We can see that the LRS resistances are almost independent with the varying of the temperature, implying a tunneling process. On the other hand, the HRS resistances increase with decreasing the temperature. For the Pt/BTO(20)/SNTO device, the HRS resistance increases about 10 times as the temperature decreases from 290 to 10 K, whereas for the Pt/BTO(0.01)/SNTO device, the HRS resistance increases about 1,000 times from 290 to 10 K. This temperature-dependent phenomenon shows a typical thermionic process at HRS. Correspondingly, as shown in Figure 4B, the ON/OFF ratios of BTO-based devices increase with decreasing temperature. We measured the evolution of the Pt/BTO(0.01)/SNTO device at various temperatures (Figure 4C). With the decrease of temperature, the negative voltage that can achieve maximum HRS resistance is almost changeless, because the pulse width is long enough for the migration of oxygen vacancies. The *I-V* hysteresis loops at 10 K are shown in Figure S13, exhibiting a giant ON/OFF ratio of 2.1×10^9.

Transport Mechanisms at Different Resistance States

To get more insight into the underlying mechanism, we further investigate the effect of the operation speed on the resistance modulation in our devices. Figure S14 shows the resistance evolution of BTO(1) using square pulses with amplitudes of −4.8 and +2.2 V. Write pulses with widths ranging from 20 ns to 0.1 s were applied to modulate the resistance states, and the resistances were read using a voltage of +0.1 V. The devices were pre-poled by applying a voltage of −4.8 V (from HRS to LRS) and +2.2 V (from LRS to HRS) with a duration of 200 ms, to ensure the same initial states. In the process from HRS to LRS, the resistance starts to change when the pulse width exceeds 10^{-7} s, corresponding to the characteristic time of the ferroelectric polarization switching (Boyn et al., 2017). The device resistance decreases rapidly as the pulse width increases, showing a sharp drop and reaching saturation around 10^{-4} s. In the process from LRS to HRS, the device resistance responses to pulses with any widths. As the pulse width rises, the device resistance increases gradually, eventually reaching saturation around 10^{-3} s. Considering that the mobility of oxygen vacancy in BTO is about 10^{-11}–10^{-12} cm^2/Vs (El Kamel and Gonon, 2006), the migration time for oxygen vacancies to move the distance of several nanometers is about 1 ms. Therefore, different switching times imply that HRS to LRS and LRS to HRS processes are dominated by ferroelectric polarization switching and oxygen vacancy migration, respectively.

Then, we analyzed *I-V* curves of BTO-based devices for both LRS and HRS. The tunneling feature at LRS was further confirmed by fitting the LRS *I-V* curve in the Pt/BTO(0.01)/SNTO device. Good agreement between the experimental data and fitting curves shows that the DT mechanism dominates the LRS in the low-bias regime and the FNT mechanism dominates the LRS in the high-bias regime (Figure S15). We estimated that the DT barrier height at Pt/BTO and BTO/SNTO interfaces are, respectively, 0.78 and 0.53 eV, and the FNT barrier height is 0.35 eV (Note S1). To exclude the possibility of the filamentary conduction, we investigated the area dependence of LRS resistances. For filamentary-type conduction, the resistance is not linearly associated with the top electrode area. In case of the interfacial-type conduction, the resistance should linearly decrease with the area (Guo et al., 2017). For the Pt/BTO(0.01)/SNTO device (Figure S16), the LRS resistance reduces exponentially as the electrode area increases exponentially, which confirms the dominant role of the interfacial-type conduction mechanism.

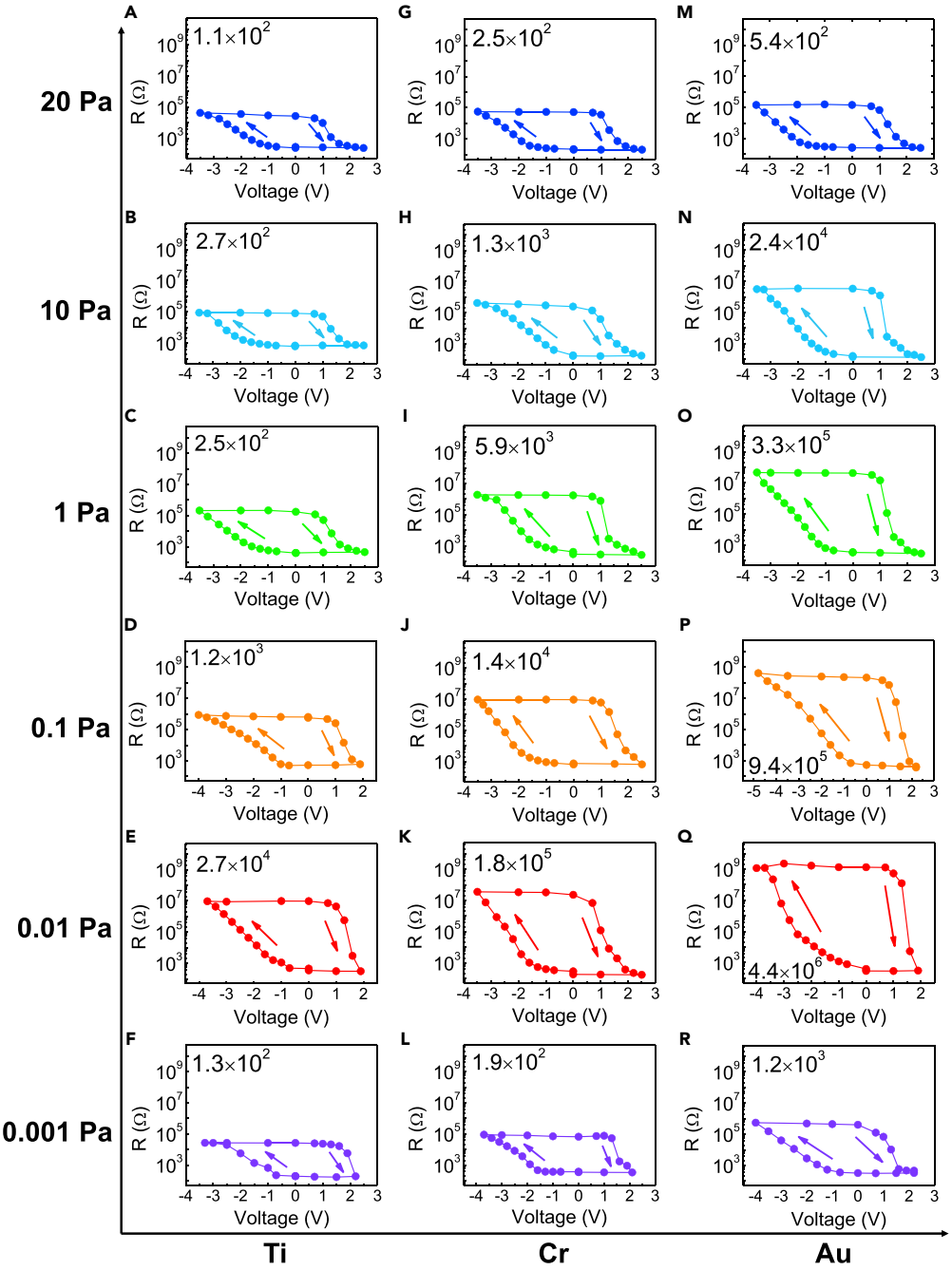

Figure 3. Resistance Switching Behavior Depending on the Top Electrode Material

Typical *R-V* loop of top electrode/BTO/SNTO tunnel junctions deposited at different oxygen pressure, where top electrode is Au (A–F), Cr/Au (G–L), and Ti/Au (M–R).

For HRS, we found that the TE model is responsible for transport by fitting the rectifying *I-V* curves of HRS via the TE model (Figure S17). The calculation details are shown in Figure S18 and Note S2. The extracted Schottky barrier height Φ_B and the corresponding ideality factor n, as a function of the deposited oxygen pressures, are plotted in Figure 4D. The Φ_B increases from 0.175 to 0.814 eV with decreasing oxygen pressure from 20 to 0.01 Pa. However, as the deposited oxygen pressure further decreases from 0.01 to 0.001 Pa, Φ_B decreases abruptly to 0.215 eV. The ideality factor n indicates the deviation of experimental results from an ideal TE (n = 1) over a Schottky barrier (Mikheev et al., 2014). Here, n decreases from 3.82 to

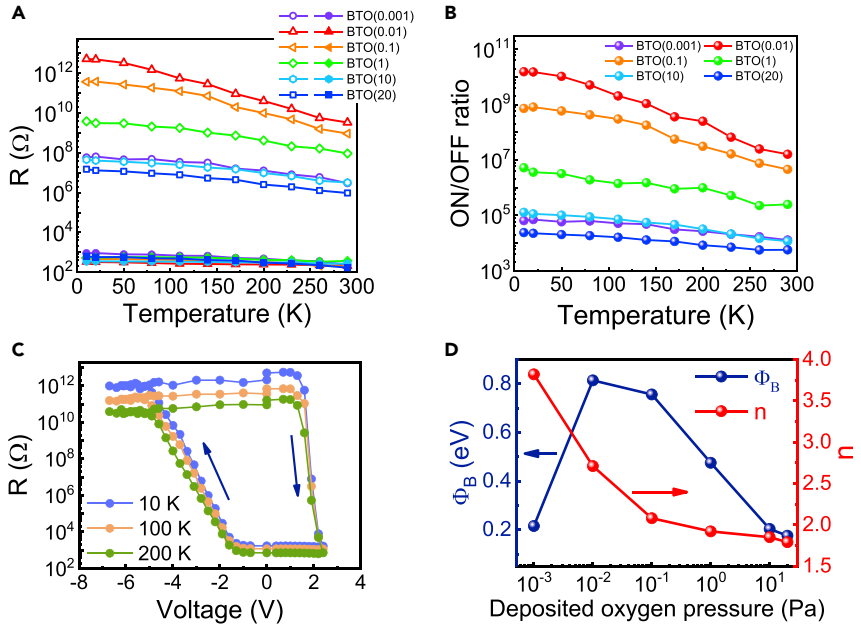

Figure 4. Temperature-Dependent Electrical Properties of BTO-Based Devices

(A) Temperature-dependent HRS and LRS resistances of the BTO-based devices.

(B) ON/OFF ratios of the BTO-based devices as a function of temperature, calculated from (A).

(C) Semi-log resistance-voltage (*R-V*) loops of Pt/BTO(0.01)/SNTO device with various temperatures for the same point. The write pulse is 200 ms. The arrows show the DC voltage scanning sequence. The read voltage is 0.1 V.

(D) Schottky barrier height (Φ_B) and ideality factor (n) of BTO-based devices as a function of the deposited oxygen pressure.

1.79 with increasing the deposited oxygen pressure from 0.001 to 20 Pa, which is usually linked to the presence of a voltage-sharing insulating interface layer (Card and Rhoderick, 1971).

Distributions of the Valence of Ti at Different Resistance States

The distributions of the Ti valence in Pt/BTO(0.01)/SNTO at both HRS and LRS were determined by the spatially resolved electron energy loss spectroscopy (EELS) (Figure S19). By fitting the EELS data with the multiple linear least-squares fitting method, we obtained the spatially resolved Ti valence data. More details on 2-D mapping of Ti valence and interface determination could be found in Figure S20. At LRS, the Ti valence is +3.5 at the Pt/BTO interface, and it gradually increases to +3.8 at the BTO/SNTO interface. At HRS, the valence of Ti is +3.1 at the Pt/BTO interface due to the $V_O^{\cdot\cdot}$ accumulation, and it subsequently increases to +3.7 at the BTO/SNTO interface. The average Ti valence at HRS is about +3.4, which is 0.3 lower than that at LRS (+3.7). The Ti valence is +4 in ideal BTO and decreases with increasing the concentration of $V_O^{\cdot\cdot}$. Therefore, the obvious change of $V_O^{\cdot\cdot}$ between LRS and HRS was confirmed by EELS measurements.

DISCUSSION

The schematic energy profiles at LRS and HRS in our FITJs can be deduced following the above-mentioned measurements (Figure 5). At LRS, the device functions as an FTJ by repelling the $V_O^{\cdot\cdot}$ from the BTO barrier into the SNTO semiconducting layer under the positive bias (Figure 5A). In this case, the DT conduction dominates the transport process of the devices. Therefore, the transport properties of BTO-based devices are nearly temperature independent. The resistance values are almost the same for all the BTO-based devices owing to the similar width and height of the tunnel barriers after repelling the $V_O^{\cdot\cdot}$. The ferroelectric polarization of the BTO barrier further reduces the barrier height and thus enhances the conduction of LRS. By comparing the BTO- and STO-based devices and confirming the ferroelectricity in the BTO(0.01) film, we can conclude that the ferroelectric polarization contributes to about one magnitude enhancement of ON/OFF ratios by decreasing the LRS resistances in BTO-based devices (Figures S4 and S5).

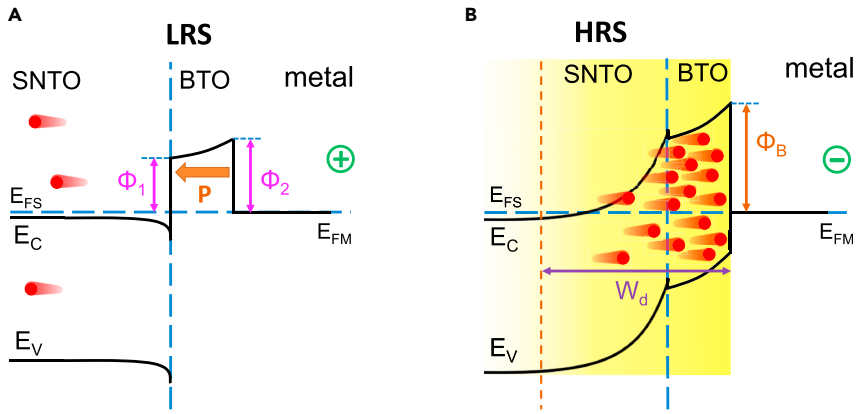

Figure 5. Energy Profiles of Pt/BTO/SNTO Ferroionic Tunnel Junctions (FITJs) in LRS and HRS Configurations

(A) Band diagram of FITJ at LRS, which is achieved by applying positive bias on the Pt electrode (represented by the green circle with plus sign). The polarization direction points to SNTO, and the oxygen vacancies (red circles) drift away from the BTO layer.

(B) Band diagram of FITJ at HRS, which is achieved by applying negative bias on the Pt electrode (represented by the green circle with minus sign). Positively charged oxygen vacancies accumulate at the barrier region, forming a Schottky barrier and increasing the width of depletion layer.

At HRS, a large amount of $V_O^{\cdot\cdot}$ accumulate near the barrier region driven by the negative bias (Figure 5B). In this case, the devices can be regarded as Schottky junctions, which is confirmed by our fitting results (Figure S17). The work function of Pt is 5.65 eV and the electron affinity of BTO is 3.9 eV, generating Schottky barrier with a height of 1.75 eV. However, the Schottky barrier height between Pt and BTO(0.01) was calculated to be 0.81 eV by analyzing the low-temperature transport data (Figure 4D), about 0.94 eV less than the theoretical barrier height. It was reported that a defect energy level within the band gap could be introduced by $V_O^{\cdot\cdot}$ depending on the defect concentration (Shanthi and Sarma, 1998). According to Lin et al. (Lin and Demkov, 2013), this in-gap level is approximately 0.4–1 eV lower than the bottom of the conduction band. The angle-resolved photoelectron spectroscopy results also showed a $V_O^{\cdot\cdot}$ -induced in-gap energy level, which is about 0.9 eV below the bottom of the conduction band (Aiura et al., 1994). Since our calculated barrier height was 0.94 eV lower than the ideal barrier height, close to the energy difference between the conduction band bottom and the $V_O^{\cdot\cdot}$-introduced in-gap level, we speculate that the $V_O^{\cdot\cdot}$-induced defect energy levels were responsible for the Schottky barrier height. $V_O^{\cdot\cdot}$ acts as an electron donor in BTO; therefore, a higher concentration of $V_O^{\cdot\cdot}$ could dope more electrons in the oxides, making the in-gap level upward and increasing the Schottky barrier height Φ_B. Thus, a larger Φ_B can be obtained in junctions fabricated under a lower oxygen pressure (Lee et al., 2014). Moreover, a larger barrier height also leads to a wider barrier width. Therefore, the accumulated $V_O^{\cdot\cdot}$ near the barrier region works to increase the height and width of Schottky barrier, leading to a sharp drop in the conductance at HRS.

The ON/OFF ratio of FITJ can reach giant values of 5.1×10^7 at room temperature and 2.1×10^9 at 10 K. To the best of our knowledge, this is the largest value to date in the literature (Figure S21). This great enhancement of ON/OFF ratio can be attributed to the coexistence of oxygen vacancy migration and ferroelectricity in the devices. We note that a recent pioneering work reported the combination of both ferroelectricity and interface oxygen vacancy migration in FTJs fabricated under high oxygen pressure (~10 Pa) containing a small amount of $V_O^{\cdot\cdot}$ (Lu et al., 2017). We investigated the effect of the deposition oxygen pressure (10^{-3}–20 Pa) on the device performance and focused on the device fabricated under low oxygen pressure (0.01 Pa) containing a large amount of $V_O^{\cdot\cdot}$. This difference makes us successfully realize a much larger ON/OFF ratio than that of about 10^3 at 10 K in their work by fully harnessing the ionic degree of freedom.

Conclusions

The results presented here demonstrate a giant electroresistance by exploiting the coupled ferroelectric-ionic states in ultrathin oxygen-deficient BTO-based FITJs. The migration of oxygen vacancies accompanying polarization reversal induced by the applied bias could effectively modify the width and height of

the interface barriers. As shown here, such interface engineering can switch the conduction mechanisms between direct tunneling and TE and thus readily provide giant resistive switching effects. The electrical manipulation of the coupled ferroelectric and ionic states in nanoscale ferroelectric oxide films offers a new direction for designing novel high-density memories.

Limitation of the Study

In this work, we deposited $BaTiO_3$ epitaxial ultrathin films on single-crystalline 0.7 wt% Nb-doped $SrTiO_3$ substrates through pulsed laser deposition technique. However, these epitaxial films are hard to be applied in existing silicon-based circuits. It would be more interesting to deposit high-quality $BaTiO_3$ epitaxial films on Si substrates and fabricate devices with high performance.

METHODS

All methods can be found in the accompanying Transparent Methods supplemental file.

SUPPLEMENTAL INFORMATION

Supplemental Information can be found online at https://doi.org/10.1016/j.isci.2019.05.043.

ACKNOWLEDGMENTS

This work was supported by National Key R&D Program of China (No. 2017YFA0303604), the National Natural Science Foundation of China (Nos. 11674385, 11404380, 11721404, and 51672007), the Youth Innovation Promotion Association of CAS (No. 2018008), the Key Research Program of Frontier Sciences CAS (No. QYZDJSSW-SLH020), and the Open Research Fund of Key Laboratory of Polar Materials and Devices Ministry of Education.

AUTHOR CONTRIBUTIONS

C.G. conceived and designed the experiments. K.J. directed the project. J.L. and H.H. fabricated samples under the supervision of C.G. J.L. carried out the device measurements under the supervision of C.G. N.L. and Y.S. performed and analyzed STEM experiments under the supervision of P.G. C.G. and J.L. wrote the manuscript with input from P.G. and N.L. All authors commented on the manuscript.

DECLARATION OF INTERESTS

The authors declare no competing interests.

Received: March 20, 2019
Revised: May 7, 2019
Accepted: May 29, 2019
Published: June 28, 2019

REFERENCES

Adepalli, K.K., Yang, J., Maier, J., Tuller, H.L., and Yildiz, B. (2017). Tunable oxygen diffusion and electronic conduction in $SrTiO_3$ by dislocation-induced space charge fields. Adv. Funct. Mater. *27*, 1700243.

Aiura, Y., Nishihara, Y., Haruyama, Y., Komeda, T., Kodaira, S., Sakisaka, Y., Maruyama, T., and Kato, H. (1994). Effect of surface oxygen vacancies on electronic states of TiO_2(110), TiO_2(001) and $SrTiO_3$(001) surfaces. Phys. B *194-196*, 1215–1216.

Asa, M., and Bertacco, R. (2018). Impact of semiconducting electrodes on the electroresistance of ferroelectric tunnel junctions. Appl. Phys. Lett. *112*, 082903.

Balke, N., Maksymovych, P., Jesse, S., Herklotz, A., Tselev, A., Eom, C.B., Kravchenko, I.I., Yu, P., and Kalinin, S.V. (2015). Differentiating ferroelectric and nonferroelectric electromechanical effects with scanning probe microscopy. ACS Nano *9*, 6484–6492.

Boyn, S., Grollier, J., Lecerf, G., Xu, B., Locatelli, N., Fusil, S., Girod, S., Carrétéro, C., Garcia, K., Xavier, S., et al. (2017). Learning through ferroelectric domain dynamics in solid-state synapses. Nat. Commun. *8*, 14736.

Card, H.C., and Rhoderick, E.H. (1971). Studies of tunnel MOS diodes I. Interface effects in silicon Schottky diodes. J. Phys. D Appl. Phys. *4*, 1589–1601.

Chanthbouala, A., Garcia, V., Cherifi, R.O., Bouzehouane, K., Fusil, S., Moya, X., Xavier, S., Yamada, H., Deranlot, C., Mathur, N.D., et al. (2012). A ferroelectric memristor. Nat. Mater. *11*, 860–864.

Christensen, D.V., von Soosten, M., Trier, F., Jespersen, T.S., Smith, A., Chen, Y., and Pryds, N. (2017). Controlling the carrier density of $SrTiO_3$-based heterostructures with annealing. Adv. Electron. Mater. *3*, 1700026.

Cooper, D., Baeumer, C., Bernier, N., Marchewka, A., La Torre, C., Dunin Borkowski, R.E., Menzel, S., Waser, R., and Dittmann, R. (2017). Anomalous resistance hysteresis in oxide ReRAM: oxygen evolution and reincorporation revealed by in situ TEM. Adv. Mater. *29*, 1700212.

Das, S., Wang, B., Cao, Y., Cho, M.R., Shin, Y.J., Yang, S.M., Wang, L., Kim, M., Kalinin, S.V., Chen, L.Q., and Noh, T.W. (2017). Controlled manipulation of oxygen vacancies using nanoscale flexoelectricity. Nat. Commun. *8*, 615.

Duan, C.G., Sabiryanov, R.F., Mei, W., Jaswal, S.S., and Tsymbal, E.Y. (2006). Interface effect on

ferroelectricity at the nanoscale. Nano Lett. *6*, 483–487.

Esaki, L., Laibowitz, R.B., and Stiles, P.J. (1971). Polar switch. IBM Tech. Discl. Bull. *13*, 2161.

Garcia, V., and Bibes, M. (2014). Ferroelectric tunnel junctions for information storage and processing. Nat. Commun. *5*, 4289.

Garcia, V., Fusil, S., Bouzehouane, K., Enouz-Vedrenne, S., Mathur, N.D., Barthélémy, A., and Bibes, M. (2009). Giant tunnel electroresistance for non-destructive readout of ferroelectric states. Nature *460*, 81–84.

Ge, C., Jin, K., Gu, L., Peng, L., Hu, Y., Guo, H., Shi, H., Li, J., Wang, J., Guo, X., et al. (2015). Metal-insulator transition induced by oxygen vacancies from electrochemical reaction in ionic liquid-gated manganite films. Adv. Mater. Interfaces *2*, 1500407.

Guo, R., Wang, Y., Yoong, H.Y., Chai, J., Wang, H., Lin, W., Chen, S., Yan, X., Venkatesan, T., Ariando, et al.. (2017). Effect of extrinsically introduced passive interface layer on the performance of ferroelectric tunnel junctions. ACS Appl. Mater. Interfaces *9*, 5050–5055.

Guo, R., Zhou, Y., Wu, L., Wang, Z., Lim, Z., Yan, X., Lin, W., Wang, H., Yoong, H.Y., Chen, S., et al. (2018). Control of synaptic plasticity learning of ferroelectric tunnel memristor by nanoscale interface engineering. ACS Appl. Mater. Interfaces *10*, 12862–12869.

Hu, W.J., Wang, Z.H., Yu, W., and Wu, T. (2016). Optically controlled electroresistance and electrically controlled photovoltage in ferroelectric tunnel junctions. Nat. Commun. *7*, 10808.

Jang, J.H., Kim, Y.M., He, Q., Mishra, R., Qiao, L., Biegalski, M.D., Lupini, A.R., Pantelides, S.T., Pennycook, S.J., Kalinin, S.V., and Borisevich, A.Y. (2017). In situ observation of oxygen vacancy dynamics and ordering in the epitaxial $LaCoO_3$ system. ACS Nano *11*, 6942–6949.

El Kamel, F., and Gonon, P. (2006). Space charge limited transient currents and oxygen vacancy mobility in amorphous $BaTiO_3$ thin films. J. Appl. Phys. *99*, 094107.

Lee, S., Lee, J.S., Park, J.B., Kyong, Y.K., Lee, M.J., and Noh, T.W. (2014). Anomalous effect due to oxygen vacancy accumulation below the electrode in bipolar resistance switching Pt/Nb:$SrTiO_3$ cells. APL Mater. *2*, 066103.

Li, C., Huang, L., Li, T., Lü, W., Qiu, X., Huang, Z., Liu, Z., Zeng, S., Guo, R., Zhao, Y., et al. (2015). Ultrathin $BaTiO_3$-based ferroelectric tunnel junctions through interface engineering. Nano Lett. *15*, 2568–2573.

Li, H.B., Lu, N., Zhang, Q., Wang, Y., Feng, D., Chen, T., Yang, S., Duan, Z., Li, Z., Shi, Y., et al. (2017b). Electric-field control of ferromagnetism through oxygen ion gating. Nat. Commun. *8*, 2156.

Li, T., Sharma, P., Lipatov, A., Lee, H., Lee, J.W., Zhuravlev, M.Y., Paudel, T.R., Genenko, Y.A., Eom, C.B., Tsymbal, E.Y., et al. (2017a). Polarization-mediated modulation of electronic and transport properties of hybrid MoS_2-$BaTiO_3$-$SrRuO_3$ tunnel junctions. Nano Lett. *17*, 922–927.

Li, Z., Guo, X., Lu, H., Zhang, Z., Song, D., Cheng, S., Bosman, M., Zhu, J., Dong, Z., and Zhu, W. (2014). An epitaxial ferroelectric tunnel junction on silicon. Adv. Mater. *26*, 7185–7189.

Lin, C., and Demkov, A.A. (2013). Electron correlation in oxygen vacancy in $SrTiO_3$. Phys. Rev. Lett. *111*, 217601.

Linn, E., Rosezin, R., Kügeler, C., and Waser, R. (2010). Complementary resistive switches for passive nanocrossbar memories. Nat. Mater. *9*, 403–406.

Lu, W., Li, C., Zheng, L., Xiao, J., Lin, W., Li, Q., Wang, X.R., Huang, Z., Zeng, S., Han, K., et al. (2017). Multi-nonvolatile state resistive switching arising from ferroelectricity and oxygen vacancy migration. Adv. Mater. *29*, 1606165.

Mikheev, E., Hoskins, B.D., Strukov, D.B., and Stemmer, S. (2014). Resistive switching and its suppression in Pt/Nb:$SrTiO_3$ junctions. Nat. Commun. *5*, 3990.

Pantel, D., and Alexe, M. (2010). Electroresistance effects in ferroelectric tunnel barriers. Phys. Rev. B *82*, 134105.

Pantel, D., Goetze, S., Hesse, D., and Alexe, M. (2012). Reversible electrical switching of spin polarization in multiferroic tunnel junctions. Nat. Mater. *11*, 289–293.

Peacock, P.W., and Robertson, J. (2002). Band offsets and Schottky barrier heights of high dielectric constant oxides. J. Appl. Phys. *92*, 4712–4721.

Qin, Q.H., Äkäslompolo, L., Tuomisto, N., Yao, L., Majumdar, S., Vijayakumar, J., Casiraghi, A., Inkinen, S., Chen, B., Zugarramurdi, A., and Puska, M. (2016). Resistive switching in all-oxide ferroelectric tunnel junctions with ionic interfaces. Adv. Mater. *28*, 6852–6859.

Rodríguez Contreras, J., Kohlstedt, H., Poppe, U., and Waser, R. (2003). Resistive switching in metal–ferroelectric–metal junctions. Appl. Phys. Lett. *83*, 4595–4597.

Scott, J.F. (2007). Applications of modern ferroelectrics. Science *315*, 954–959.

Shanthi, N., and Sarma, D.D. (1998). Electronic structure of electron doped $SrTiO_3$: $SrTiO_{3-\delta}$ and $Sr_{1-x}La_xTiO_3$. Phys. Rev. B *57*, 2153.

Soni, R., Petraru, A., Meuffels, P., Vavra, O., Ziegler, M., Kim, S.K., Jeong, D.S., Pertsev, N.A., and Kohlstedt, H. (2014). Giant electrode effect on tunneling electroresistance in ferroelectric tunnel junctions. Nat. Commun. *5*, 5414.

Tsymbal, E.Y., and Kohlstedt, H. (2006). Tunneling across a ferroelectric. Science *313*, 181–183.

Waser, R., Dittmann, R., Staikov, G., and Szot, K. (2009). Redox-based resistive switching memories - nanoionic mechanisms, prospects, and challenges. Adv. Mater. *21*, 2632–2663.

Wen, Z., Li, C., Wu, D., Li, A., and Ming, N. (2013). Ferroelectric-field-effect-enhanced electroresistance in metal/ferroelectric/semiconductor tunnel junctions. Nat. Mater. *12*, 617–621.

Xi, Z., Ruan, J., Li, C., Zheng, C., Wen, Z., Dai, J., Li, A., and Wu, D. (2017). Giant tunnelling electroresistance in metal/ferroelectric/semiconductor tunnel junctions by engineering the Schottky barrier. Nat. Commun. *8*, 15217.

Yang, S.M., Morozovska, A.N., Kumar, R., Eliseev, E.A., Cao, Y., Mazet, L., Balke, N., Jesse, S., Vasudevan, R.K., Dubourdieu, C., and Kalinin, S.V. (2017). Mixed electrochemical-ferroelectric states in nanoscale ferroelectrics. Nat. Phys. *13*, 812–818.

Yao, L., Inkinen, S., and van Dijken, S. (2017). Direct observation of oxygen vacancy-driven structural and resistive phase transitions in $La_{2/3}Sr_{1/3}MnO_3$. Nat. Commun. *8*, 14544.

Yao, L., Majumdar, S., Äkäslompolo, L., Inkinen, S., Qin, Q.H., and Dijken, van S. (2014). Electron-beam-induced Perovskite-Brownmillerite-Perovskite structural phase transitions in epitaxial $La_{2/3}Sr_{1/3}MnO_3$ films. Adv. Mater. *26*, 2789–2793.

Yau, H.M., Xi, Z., Wen, Z., Wu, G., and Dai, J.Y. (2017). Dynamic strain-induced giant electroresistance and erasing effect in ultrathin ferroelectric tunnel-junction memory. Phys. Rev. B *95*, 214304.

Yin, Y.W., Burton, J.D., Kim, Y.-M., Borisevich, A.Y., Pennycook, S.J., Yang, S.M., Noh, T.W., Gruverman, A., Li, X.G., Tsymbal, E.Y., and Li, Q. (2013). Enhanced tunnelling electroresistance effect due to a ferroelectrically induced phase transition at a magnetic complex oxide interface. Nat. Mater. *12*, 397–402.

Yoon, C., Lee, J.H., Lee, S., Jeon, J.H., Jang, J.T., Kim, D.H., Kim, Y.H., and Park, B.H. (2017). Synaptic plasticity selectively activated by polarization-dependent energy-efficient ion migration in an ultrathin ferroelectric tunnel junction. Nano Lett. *17*, 1949–1955.

Zhang, T.J., Pan, R.K., Ma, Z.J., Duan, M.G., Wang, D.F., and He, M. (2011). Large rectifying leakage current in Pt/$BaTiO_3$/Nb:$SrTiO_3$/Pt structure. Appl. Phys. Lett. *99*, 182106.

Zenkevich, A., Minnekaev, M., Matveyev, Y., Levedinskii, Y., Bulakh, K., Chouprik, A., Baturin, A., Maksimova, K., Thiess, S., and Drube, W. (2013). Electronic band alignment and electron transport in Cr/$BaTiO_3$/Pt ferroelectric tunnel junctions. Appl. Phys. Lett. *102*, 062907.

Zhuravlev, M.Y., Sabirianov, R.F., Jaswal, S.S., and Tsymbal, E.Y. (2005). Giant electroresistance in ferroelectric tunnel junctions. Phys. Rev. Lett. *94*, 246802.

ISCI, Volume *16*

Supplemental Information

Giant Electroresistance in Ferroionic Tunnel Junctions

Jiankun Li, Ning Li, Chen Ge, Heyi Huang, Yuanwei Sun, Peng Gao, Meng He, Can Wang, Guozhen Yang, and Kuijuan Jin

Supplemental Figures

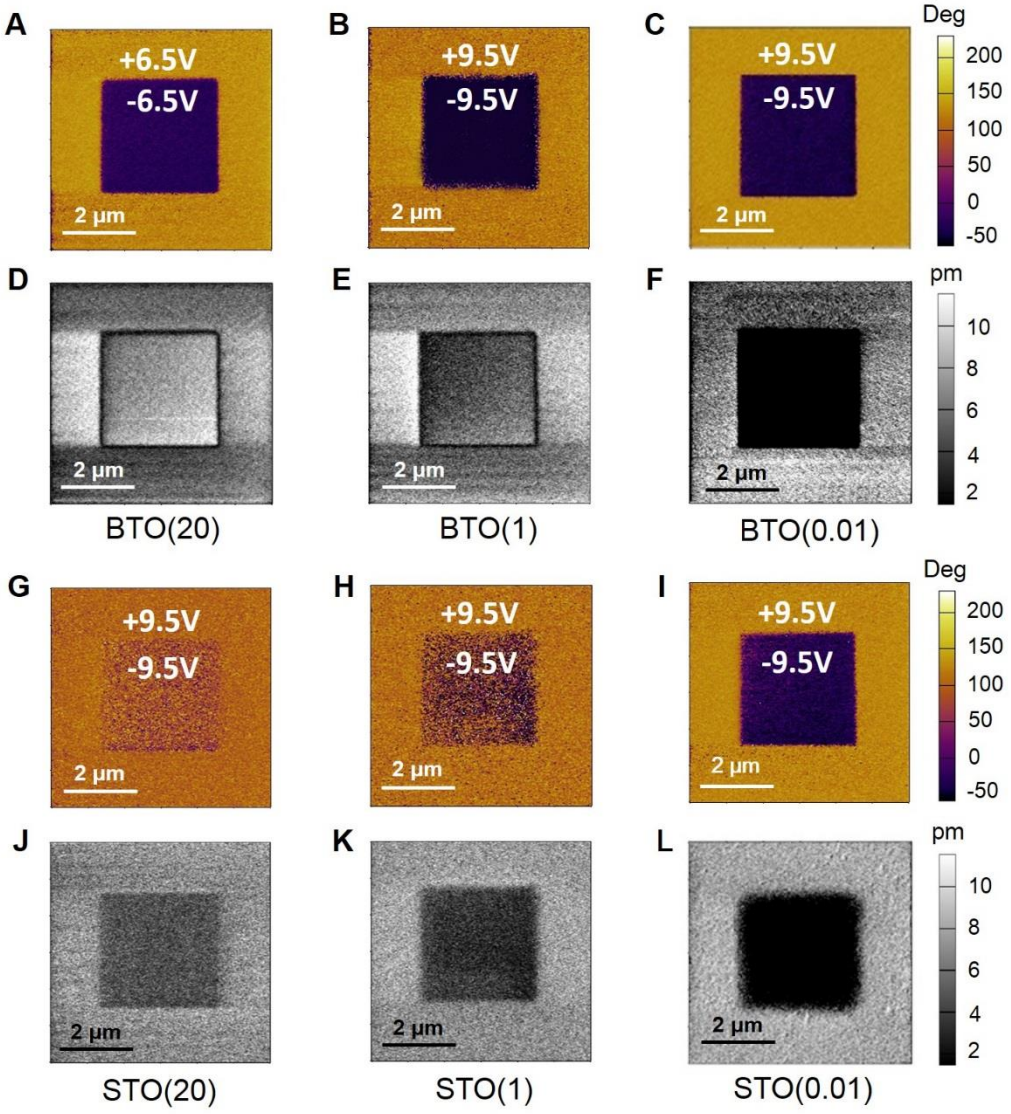

Figure S1, related to Figure 1. PFM out-of-plane phase images and the corresponding amplitude images of BTO and STO based devices. BTO(O_p) (STO(O_p)) notation denote the BTO (STO) ultrathin films fabricated under O_p Pa oxygen pressure. PFM out-of-plane phase images and corresponding amplitude images are obtained on BTO/SNTO (A-F) and STO/SNTO (G-L) heterostructures after applying an external voltage of +6.5 V (+9.5 V) to a square of 6×6 μm^2 and -6.5 V (-9.5 V) to a square of 3 × 3 μm^2 inside it. Large writing voltages (±9.5 V) for PFM measurements are utilized to ensure the migration and accumulation of oxygen vacancies during the tip scanning.

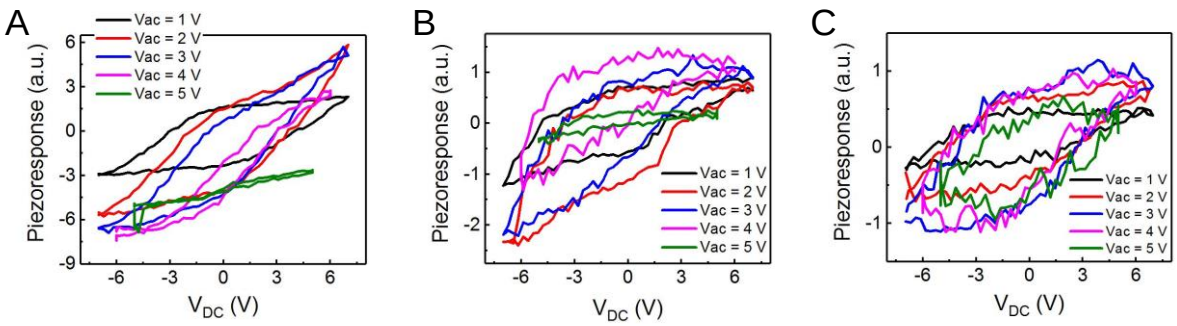

Figure S2, related to Figure 1. Off-field out-of-plane PFM response hysteresis loops with various AC voltages of BTO(20) (A), BTO(0.01) (B) and STO(0.01) (C), respectively. The PFM hysteresis loops starts to reduce and eventually collapse with the increasing of AC voltage, confirming a robust ferroelectricity of BTO(20) (Balke et al., 2015). The PFM response of BTO(0.01) is reduced compared with that of BTO(20), which is attributed to the weakening of ferroelectricity by oxygen vacancies. Significant attenuation and collapse of the PFM amplitude can also occur in BTO(0.01). An electrochemical process induced piezoresponse was observed in STO(0.01).

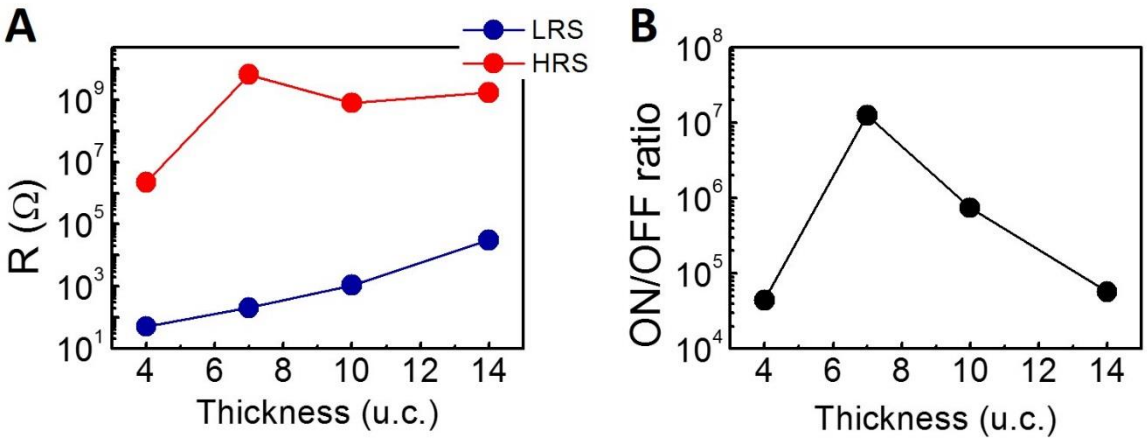

Figure S3, related to Figure 2. Resistances at high resistance (HRS) and low resistance state (LRS) (A) and corresponding ON/OFF ratios (B) for Pt/BTO/SNTO tunnel junctions as a function of BTO layer thickness, which ranged from 4 to 14 u.c.. The deposited oxygen pressure was 0.01 Pa.

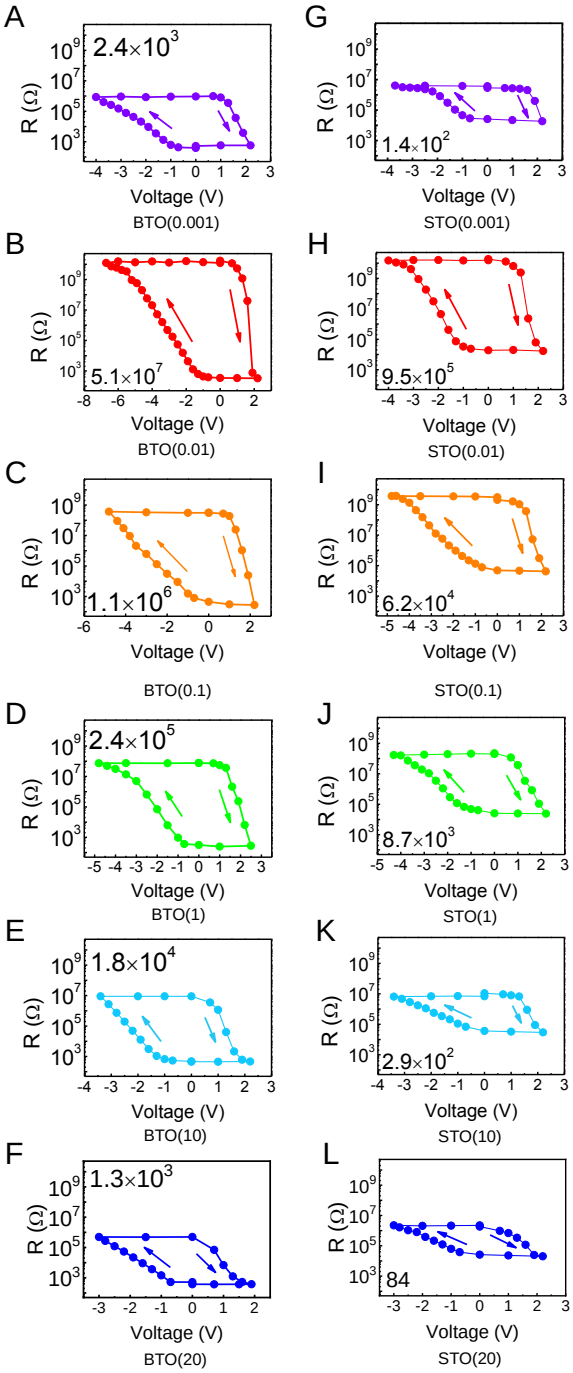

Figure S4, related to Figure 2. Typical resistance-voltage (*R*-*V*) hysteresis loops of BTO (A-F) and STO (G-L) based devices. The corresponding ON/OFF ratios are indicated in each panel. The arrows exhibit the direction of the pulse sequence.

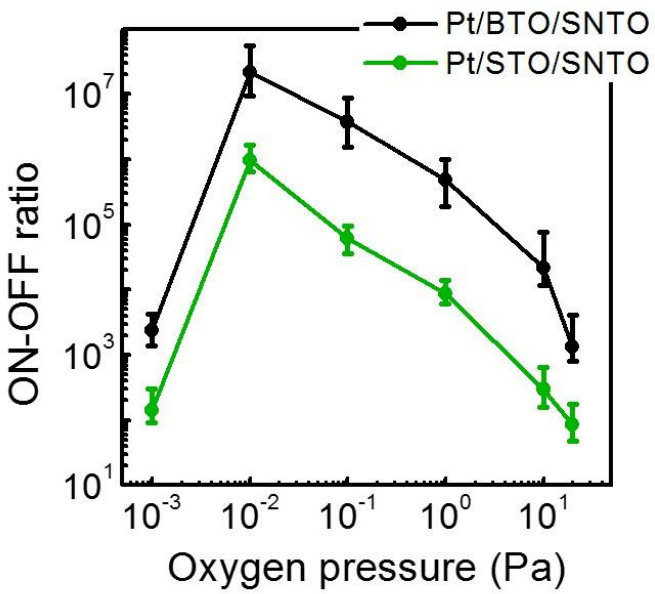

Figure S5, related to Figure 2. ON/OFF ratios of BTO and STO based devices calculated from Figure 2B. The error bars correspond to deviations of 10 devices.

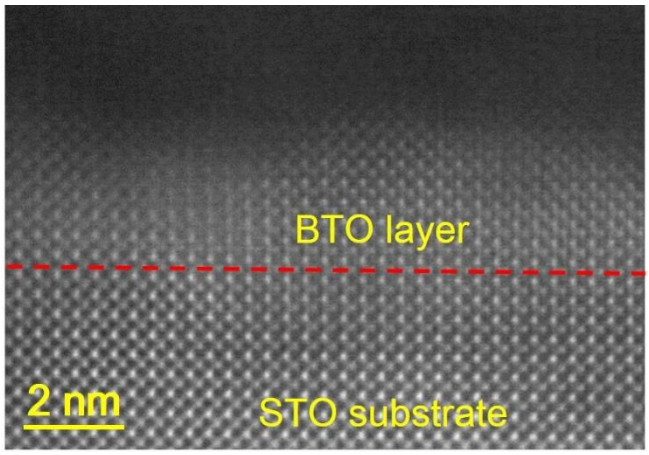

Figure S6, related to Figure 2. A cross-sectional high angle annular dark field (HAADF) image of Pt/BTO(0.001)/SNTO device. The blurring of the atomic points indicates a large structural distortion induced by a large amount of oxygen vacancies.

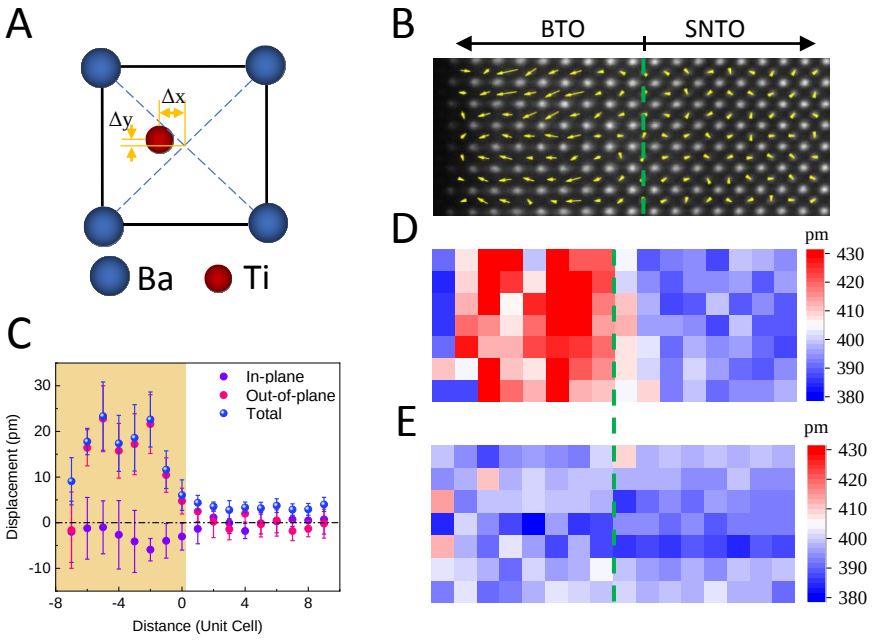

Figure S7, related to Figure 2. Quantitative measurements of atomic displacement in BTO(0.01). (A) Schematic shows the calculated center-displacement of Ti atoms. (B) A HAADF image of the pristine BTO(0.01) film shows the distribution of center-displacements. The TiO_2 plane between the BaO and SrO planes is labelled as the interface. The direction of arrows denotes the polarization direction and the length of arrows denotes the relative values. (C) Quantitative values of atomic displacements. The error bars are defined by the standard deviation (s.d.). (D-E) Lattice spacing at out-of-plane direction (D) and in-plane direction (E), respectively.

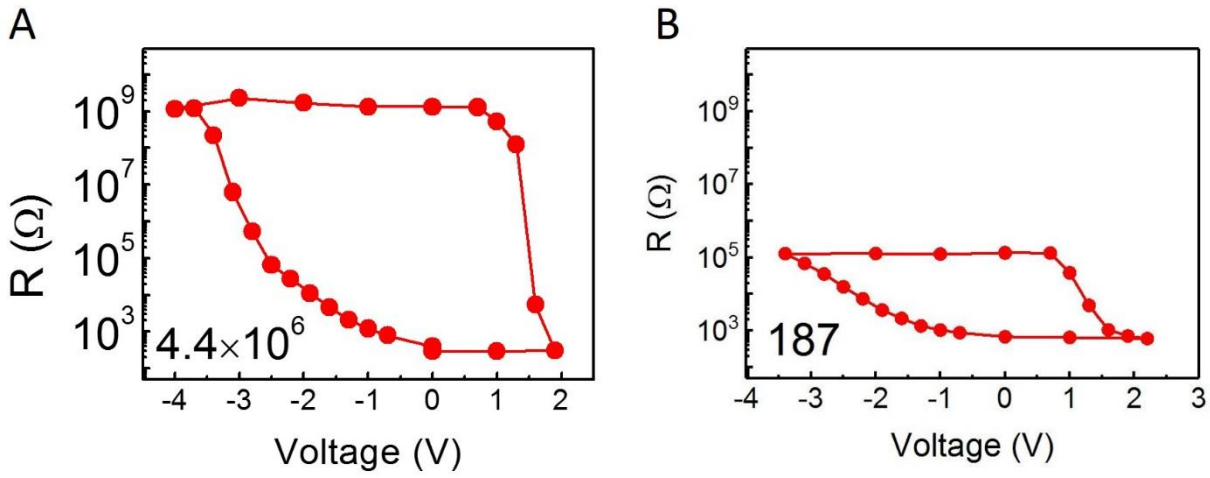

Figure S8, related to Figure 2. *R-V* loops of Au/BTO (0.01)/SNTO (A) and Au/annealed BTO(0.01)/SNTO (B).

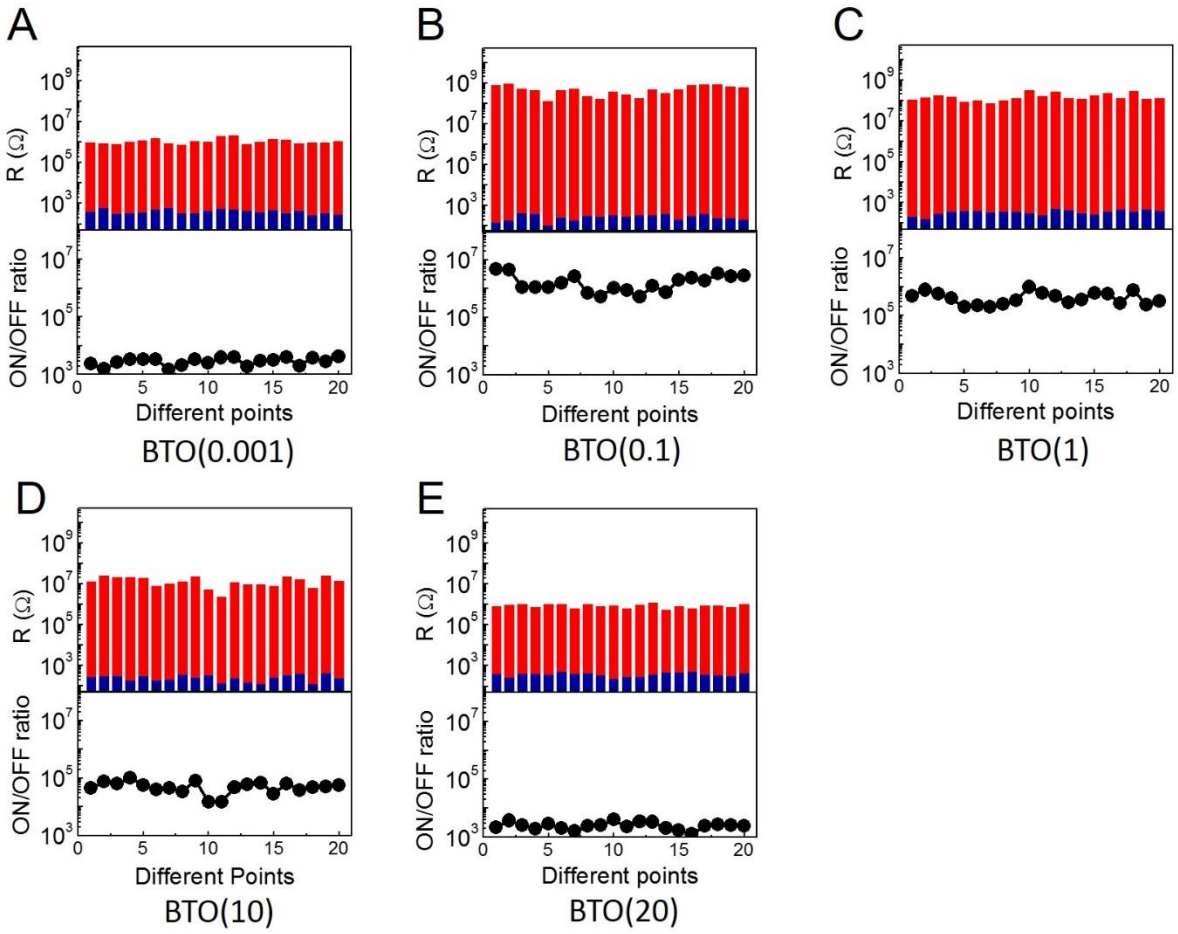

Figure S9, related to Figure 2. LRS (dark blue) and HRS (red) resistances (upper panel) and the corresponding ON/OFF ratios (bottom panel) of 20 different memory cells for BTO based devices. The read voltage is 0.1 V. The results demonstrate that our devices are uniform and reproducible.

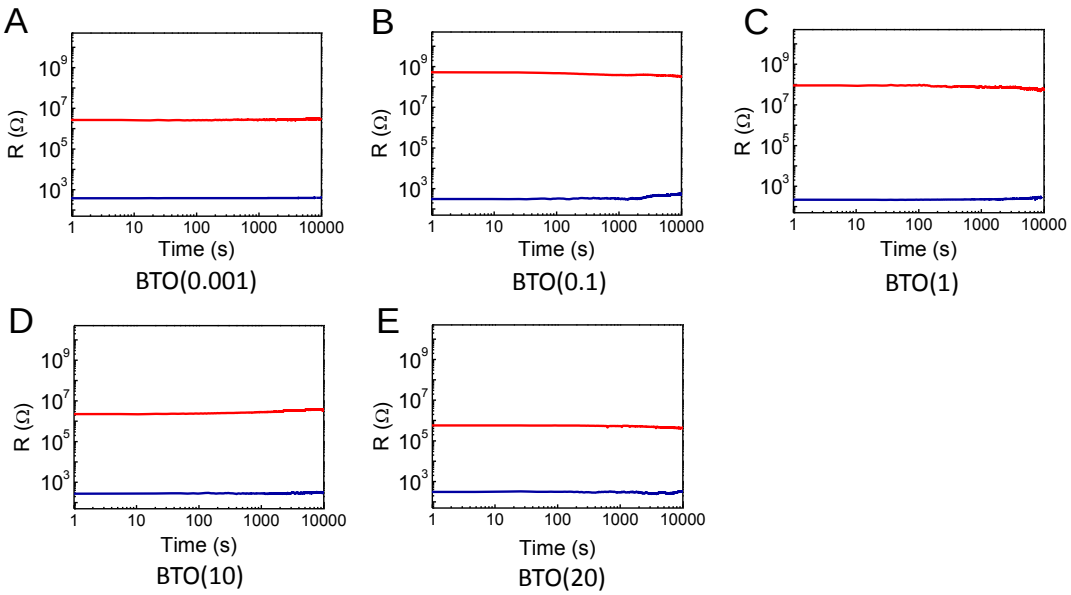

Figure S10, related to Figure 2. Retention properties of the 7 u.c.-thick Pt/BTO/SNTO films with various deposited oxygen pressures from 0.001 Pa to 20 Pa, respectively. The HRS and LRS are measured as a function of time at a read voltage of 0.1 V.

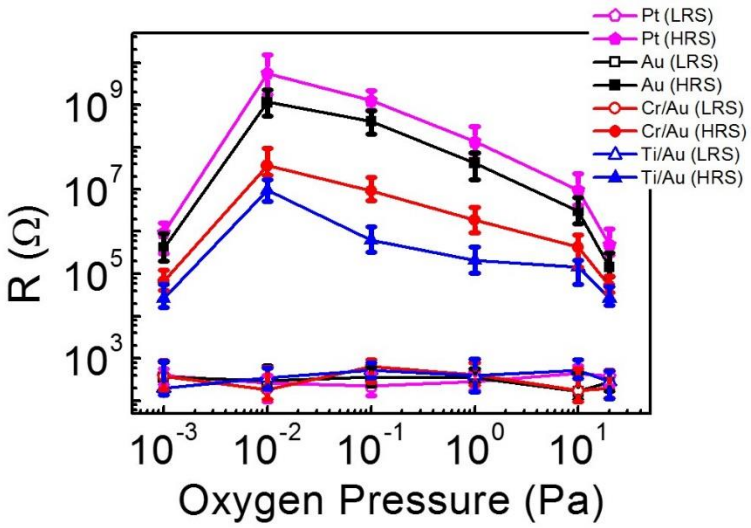

Figure S11, related to Figure 3. HRS and LRS resistances of top electrode/BTO/SNTO thin films with different top electrodes as a function of different deposited oxygen pressure at room temperature. Solid symbols represent the HRS resistances while open symbols represent LRS resistances. The vertical error bars correspond to deviations of resistance from 10 devices.

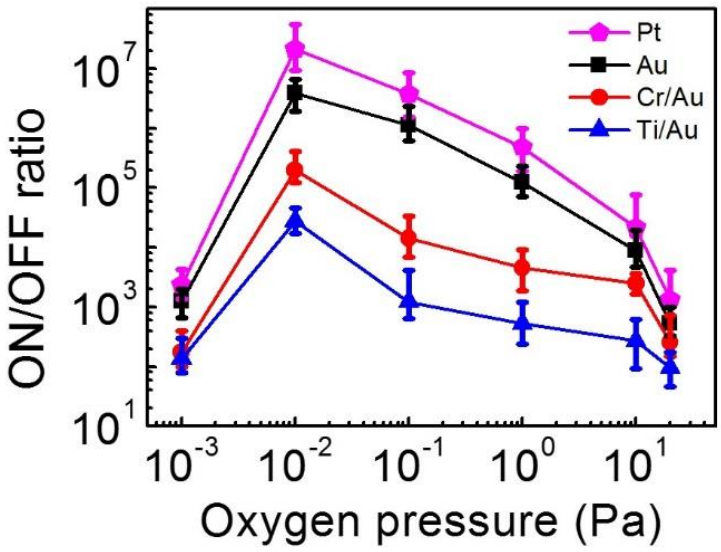

Figure S12, related to Figure 3. ON/OFF ratios of top electrodes/BTO/SNTO thin films as a function of different deposited oxygen pressures. The vertical error bars correspond to deviations of 10 devices.

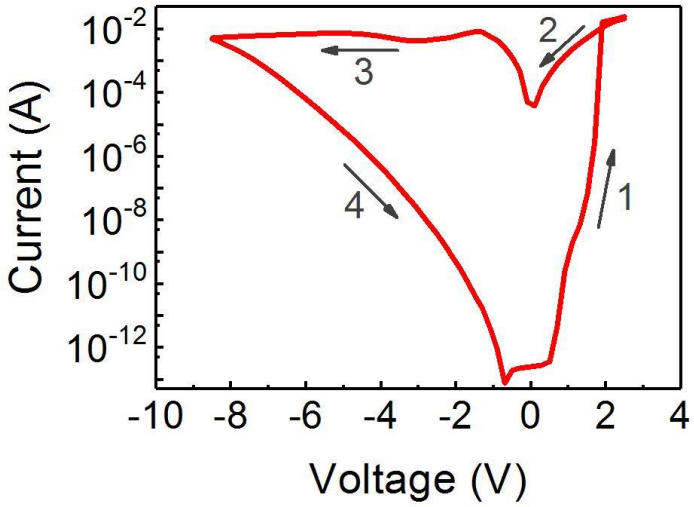

Figure S13, related to Figure 4. A typical current-voltage **(***I*-*V*) loop of Pt/BTO(0.01)/SNTO devices at 10 K.

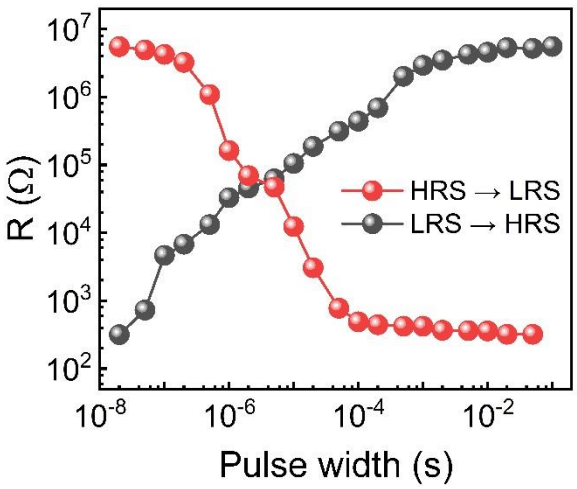

Figure S14, related to Figure 5. The resistance evolution of BTO(1) with writing pulse widths ranging from 20 ns to 0.1 s. Write voltages +2.2 V and -4.8 V were applied for HRS to LRS and LRS to HRS process, respectively. All measurement data have the same initial resistance states and are excited by a single pulse. Different switching times for HRS to LRS and LRS to HRS imply that they are driven by different mechanisms.

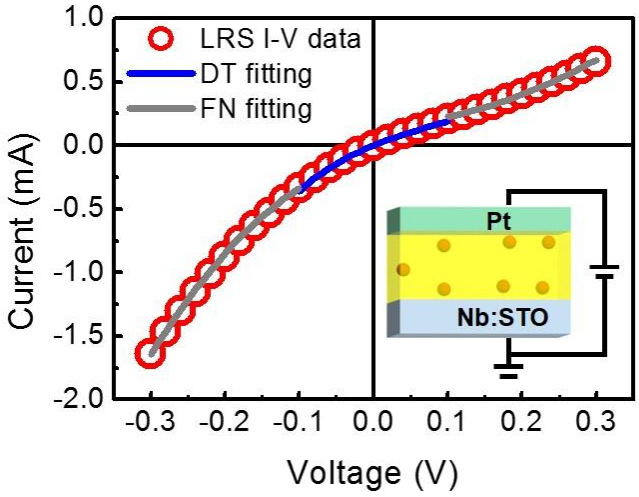

Figure S15, related to Figure 5. Measured and fitted *I-V* curve of LRS for BTO based junctions. Red open circles, blue lines and grey lines denote measured data, direct tunneling fitting and FN fitting, respectively. Inset: Schematic of the device configuration, oxygen vacancy content and bias direction at LRS.

Note S1, related to Figure 5.

The nonlinear LRS *I-V* curves at low voltage can be well fitted by the direct tunneling (DT) theory (Gruverman et al., 2009). The direct tunneling current I_{DC} through a trapezoidal barrier can be described by

$$I_{DC} = -S\frac{4em^*}{9\pi^2\hbar^3}\frac{\exp\{\alpha(V)[(\Phi_2-\frac{eV}{2})^{\frac{3}{2}}-(\Phi_1+\frac{eV}{2})^{\frac{3}{2}}]\}}{\alpha^2[(\Phi_2-\frac{eV}{2})^{\frac{1}{2}}-(\Phi_1+\frac{eV}{2})^{\frac{1}{2}}]^2}\times\sinh\{\frac{3}{2}\alpha(V)[(\Phi_2-\frac{eV}{2})^{\frac{1}{2}}-(\Phi_1+\frac{eV}{2})^{\frac{1}{2}}]\frac{eV}{2}\} \quad (1)$$

where $\alpha = \frac{4d(2m^*)^{\frac{1}{2}}}{3\hbar(\Phi_1+eV-\Phi_2)}$, Φ_1 and Φ_2 are the barrier height at Pt/BTO and BTO/SNTO interface, respectively. S is the junction area, m* is the effective electron mass, ħ is the reduced Planck constant and d is the BTO barrier width of about 2.8 nm. Here, Φ_1 and Φ_2 are used as fit parameters to describe the direct tunnelling through a trapezoidal potential barrier. The calculated Φ_1 and Φ_2 are 0.78 eV and 0.53 eV.

The Fowler-Nordheim (FN) tunneling corresponds to electrodes tunneling across a triangular-shaped potential barrier, when an electrical field E is applied to a rectangular or trapezoidal barrier (Pantel et al., 2010). The current is given by:

$$I_{FN} = S\frac{e^3}{8\pi h\Phi_i}(\frac{V}{d})^2 \exp[-\frac{8\pi\sqrt{2m^*}d\Phi_i^{\frac{3}{2}}}{3heV}] \tag{2}$$

where Φ_i is the height of trapezoidal barrier.

Equation (2) can be rewritten as:

$$\ln(\frac{I_{FN}}{V^2}) = \ln S + \ln A - k(\frac{1}{V}) \tag{3}$$

where $A = \frac{e^3}{8\pi hd^2\Phi_i}$, $k = \frac{8\pi\sqrt{2m^*}d\Phi_i^{\frac{3}{2}}}{3he}$.

It can be deduced from Equation (3) that, in FN model, $\ln(I_{FN}/V^2)$ versus (1/V) curve shows a linear dependence at high voltage. In our experiment, we estimate that the voltage shreshold for transition from DT to FNT start at a voltage higher than ±0.1 V. According to the fitting results of the FN model, Φ_i was found to be 0.35 eV for BTO based devices.

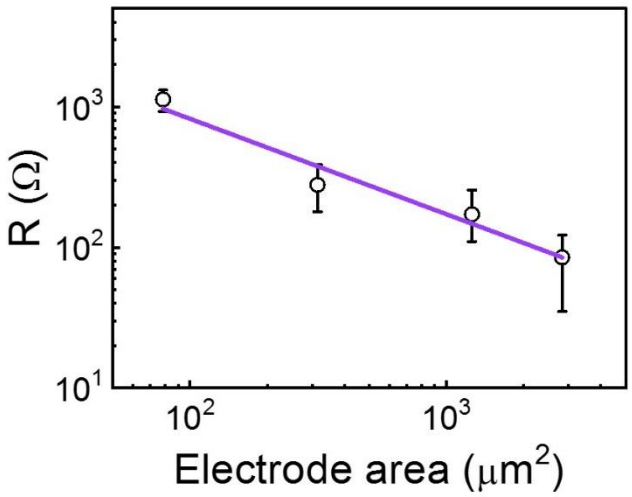

Figure S16, related to Figure 5. LRS resistances of Pt/BTO(0.01)/SNTO devices as a function of circular electrode sizes. The error bars correspond to deviations of resistance from 10 devices.

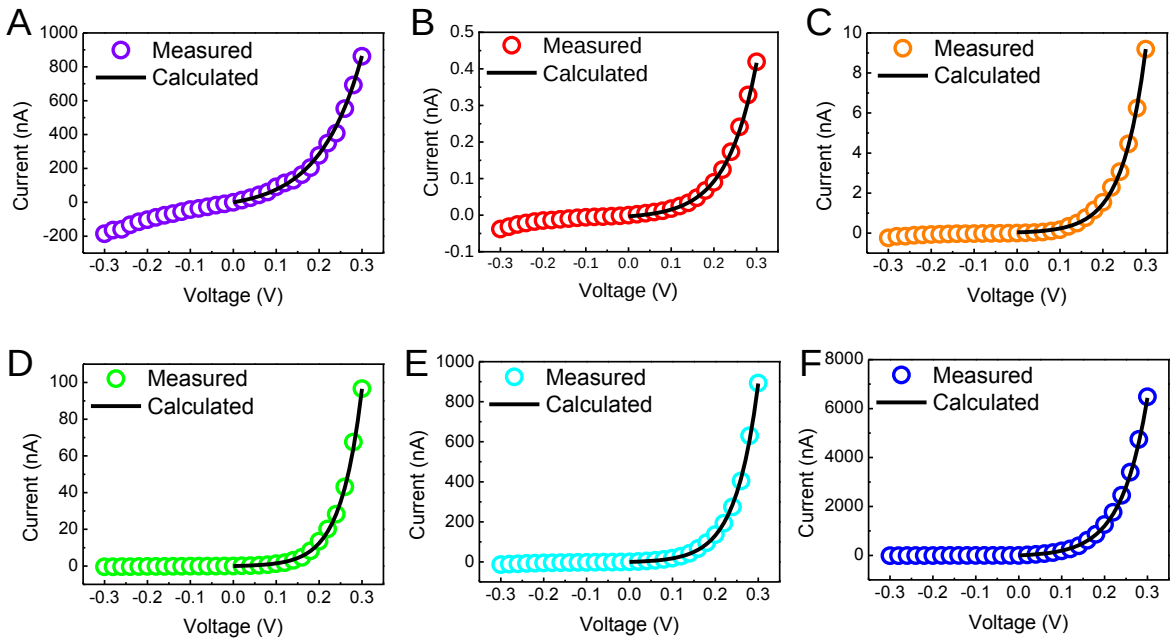

Figure S17, related to Figure 5. Fittings to the HRS *I-V* curves of BTO(0.001) (A), BTO(0.01) (B), BTO(0.1) (C), BTO(1) (D) BTO(10) (E) and BTO(20) (F) sandwiched by Pt and SNTO electrodes. Inset in (B): Schematic of the device configuration, oxygen vacancy content and bias direction at HRS.

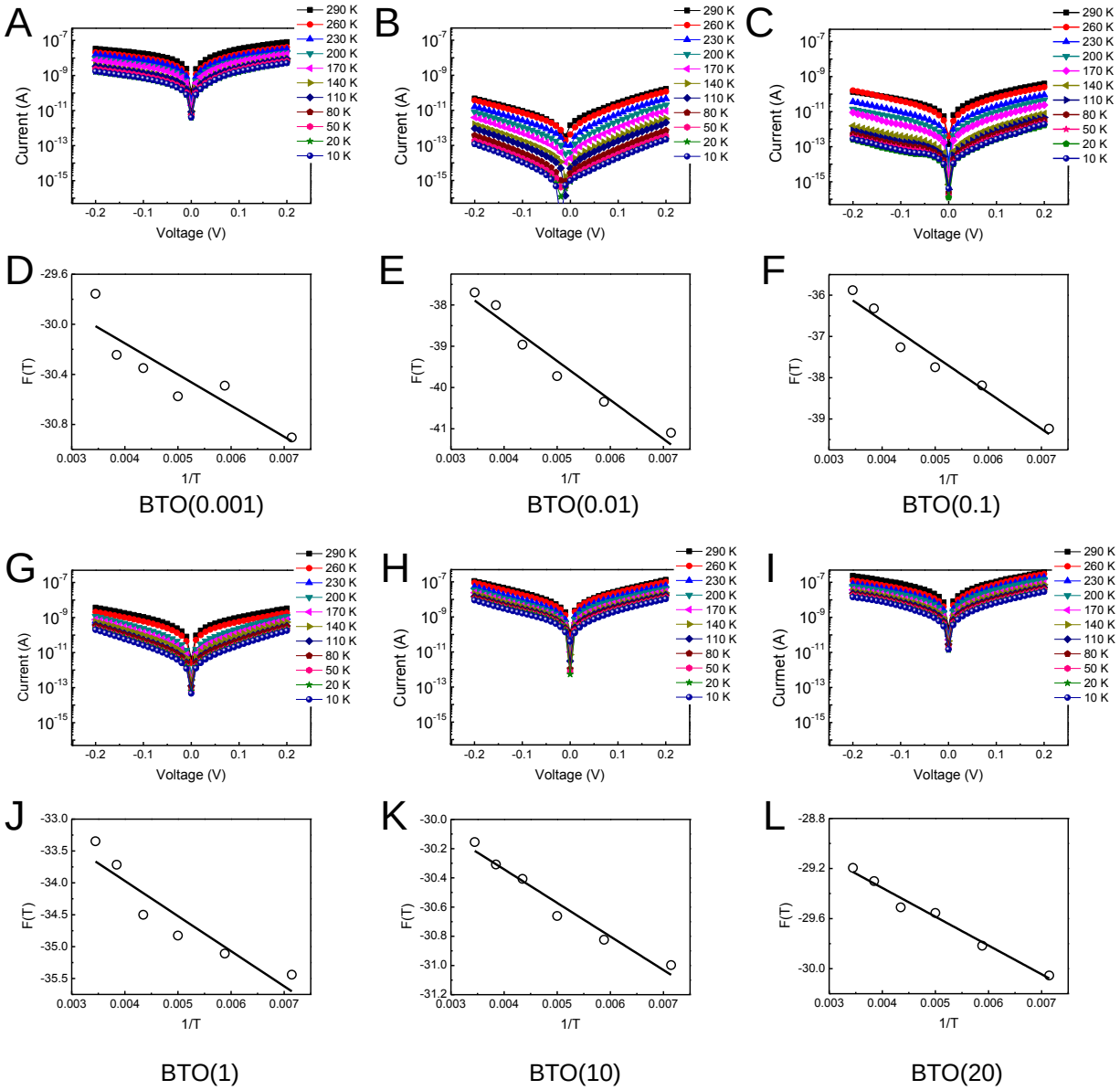

Figure S18, related to Figure 5. *I-V* curves (A-C, G-I) and F(T)-1/T plots (D-F, J-L) of the corresponding *I-V* data measured for Pt/BTO(0.001)/SNTO to Pt/BTO(20)/SNTO junctions at HRS at different temperatures, where the lines fit the F(T)-1/T curves in (D-F, J-L).

Note S2, related to Figure 5.

For the thermionic emission (TE) currents, under forward bias ($V > 3k_BT/q$), the current across the Schottky barrier is given by

$$I = SA^{*}T^{2}\theta_{n}\exp(-\frac{\Phi_{B}}{k_{B}T})\exp(\frac{qV}{nk_{B}T}) \tag{4}$$

where A* is the standard Richardson constant, Φ_B is the Schottky barrier height, T is the temperature, k_B is the Boltzmann's constant and n is the ideality factor.

Equation (4) can be rewritten as:

$$\ln(\frac{I}{T^{2}}) = \ln(SA^{*}\theta_{n}) - \frac{\Phi_{B}}{k_{B}T} + \frac{qV}{nk_{B}T} \tag{5}$$

For a given T, the $\ln(I/T^2)$ scales in approximate linearity with V, consistent with equation (5). If the overall current originates purely from the thermionic emission, the $\ln(J/T^2)$-V slope would be reciprocal to T according to equation (5). The fact that the $\ln (J/T^2)$-V curves at different T remain largely parallel suggests non-negligible contribution from the tunneling current. In this case, the ideality factor n should be modified to account for the tunneling contribution, so that the thermionic emission theory is still applicable. To extract parameter Φ_B, one may turn to the intercept of the $\ln (J/T^2)$-V curve on the vertical axis (V=0):

$$F(T) = \ln(SA^{*}\theta_{n})) - \frac{\Phi_{B}}{k_{B}T} \tag{6}$$

Then, F(T) vs. (1/V) is linear with a slope equal to $-\frac{\Phi_{B}}{k_{B}}$.

For the BTO based devices, we showed the temperature dependent *I-V* characteristics of HRS and the corresponding F(T) vs. (1/T) fitting curves of BTO based devices from 290 K to 10 K (Figure S18). In the calculations, $A^*=156$ A cm^{-2} K^{-2} and $m^*=0.12$ m_0. The linear fitting gives the value of Φ_B of different devices. In addition, n can be calculated by Equation (5).

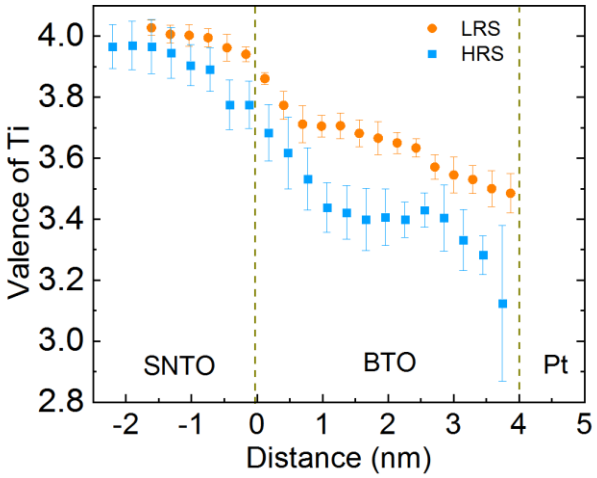

Figure S19, related to Figure 5. Distribution of the Ti valence at HRS and LRS in the Pt/BTO(0.01)/SNTO device. Orange dots and blue squares represent the Ti valence distribution at LRS and HRS, respectively. Two dashed lines denote the interfaces which are distinguished by M edge intensity of Ba-M edge. The error bars are defined by the s.d.

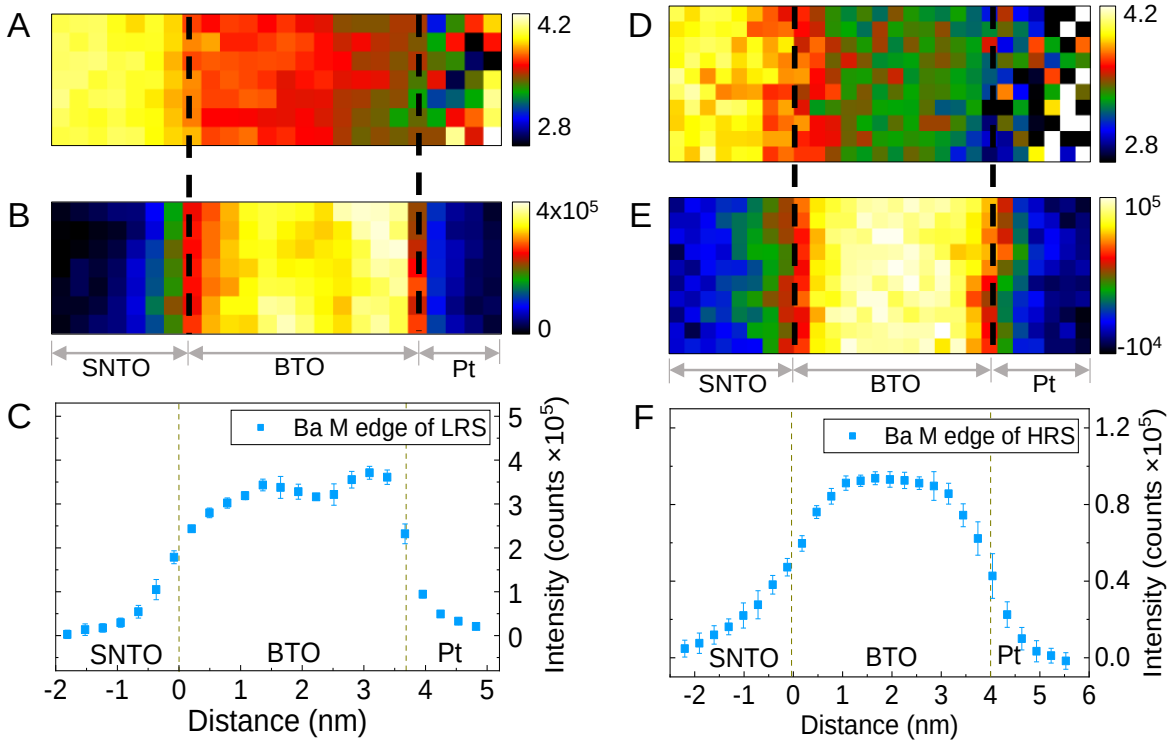

Figure S20, related to Figure 5. 2-D mapping of Ti valence and Ba-M edge intensity at LRS and HRS in the Pt/BTO(0.01)/SNTO device. (A) 2-D mapping of the Ti valence distribution at LRS. The Ba-M edge intensity mapping (B) and line profile (C) of the LRS sample, which are used to locate the interfaces. (D) 2-D mapping of the Ti valence distribution at HRS. The Ba-M edge intensity mapping (E) and line profile (F) of HRS sample, which are used to locate the interfaces. The error bars in (C) and (F) are defined by the s.d.

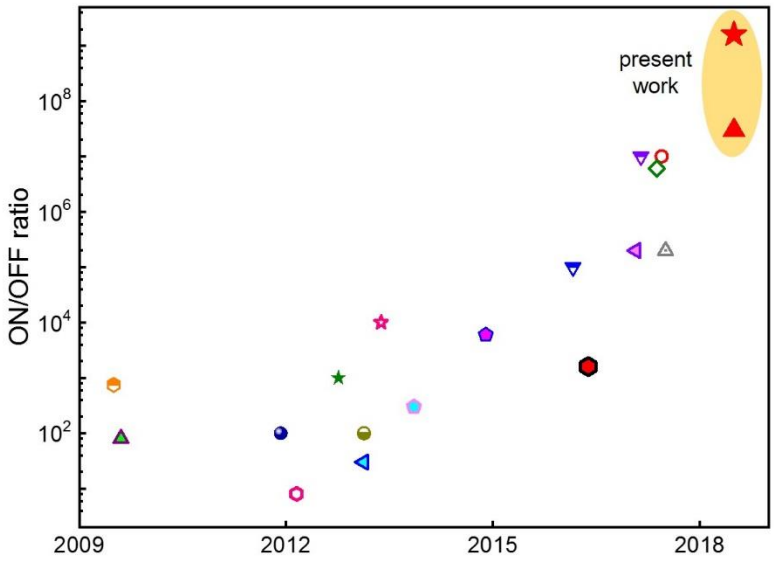

- $BaTiO_3$ (3 nm) - $La_{0.67}Sr_{0.33}MnO_3$ - $NdGaO_3$ (Garcia et al., 2009)
- $BaTiO_3$ (4.8 nm) - $SrRuO_3$ - $SrTiO_3$ (Gruverman et al., 2009)
- Au/Co - $BaTiO_3$ (2 nm) $La_{0.67}Sr_{0.33}MnO_3$ - $NdGaO_3$ (Chanthbouala et al., 2011)
- Au/Co - $PbZr_{0.2}Ti_{0.8}O_3$ (3.2 nm) - $La_{0.7}Sr_{0.3}MnO_3$ - $SrTiO_3$ (Pantel et al., 2012)
- Au/Co - $BaTiO_3$ (4 u.c. - 7 u.c.) - $La_{0.67}Sr_{0.33}MnO_3$ - $NdGaO_3$ (Kim et al., 2012)
- Cr - $BaTiO_3$ (2-15 nm) - Pt (10-15 nm) - MgO (Zenkevich et al., 2013)
- Au/Cr - $La_{0.7}Sr_{0.3}MnO_3$ - $La_{0.5}Ca_{0.5}MnO_3$ - $BaTiO_3$ (3 nm) - $La_{0.7}Sr_{0.3}MnO_3$ - $SrTiO_3$ (Yin et al., 2013)
- Pt - $BaTiO_3$ (7 u.c.) - Nb-doped $SrTiO_3$ (Wen et al., 2013)
- $PbZr_{0.2}Ti_{0.8}O_3$ - $La_{1-x}Sr_xMnO_3$ - $SrTiO_3$ (Jiang et al., 2013)
- Graphene - $BaTiO_3$ (6 u.c.) - $La_{0.67}Sr_{0.33}MnO_3$ - $SrTiO_3$ (Lu et al., 2014)
- ITO/Pt - $Sm_{0.1}Bi_{0.9}FeO_3$ (3-9 nm) - Nb-doped $SrTiO_3$ (Hu et al., 2016)
- Au/Ti - $BaTiO_3$ (6 u.c.) - $SrTiO_3$ (4 u.c.) $SrRuO_3$ - $SrTiO_3$ (Wang et al., 2016)
- Pt - $BaTiO_3$ (5 u.c.) - Nb-doped $SrTiO_3$ (Guo et al., 2017)
- Ag - $PbZr_{0.52}Ti_{0.48}O_3$ (4nm) - $La_{0.8}Sr_{0.2}MnO_3$ - $SrTiO_3$ (Yoon et al., 2017)
- Pt - $BaTiO_3$ (4u.c.) - Nb-doped $SrTiO_3$(0.1wt%) (Xi et al., 2017)
- Pt - $BaTiO_3$ (4 u.c.) - Nb-doped $SrTiO_3$ (Yau et al., 2017)
- Au - $BaTiO_3$ (7 nm) - Nb-doped $SrTiO_3$ (Fan et al., 2017)
- Pt - $BaTiO_3$ (7 u.c., 0.01 Pa) - Nb-doped $SrTiO_3$ at room temperature
- Pt - $BaTiO_3$ (7 u.c., 0.01 Pa) - Nb-doped $SrTiO_3$ at 10 K

Figure S21, related to Figure 5. ON/OFF ratio timeline for ferroelectric tunnel junctions. Our experimental data for Pt/BTO(0.01)/SNTO device measured at room temperature (red circle) and 10 K (red pentagram) show the highest ON/OFF ratio.

Transparent Methods

Film Growth

Epitaxial single-crystalline $BaTiO_3$ (BTO) and $SrTiO_3$ (STO) films were grown by pulsed laser deposition (PLD) on (001)-oriented 0.7 wt% Nb-doped $SrTiO_3$ substrates using a XeCl (λ=308 nm) excimer laser with an energy density of 2.5 J cm^{-2} and a repetition rate of 2 Hz. BTO and STO films were deposited at 750 ℃ in a flowing oxygen atmosphere of various oxygen pressures (0.001 Pa, 0.01 Pa, 0.1 Pa, 1 Pa, 10 Pa and 20 Pa) and cooled down to room temperature at 20 ℃ min^{-1}. The deposition rates of oxide films deposited at different oxygen pressures were calibrated by X-ray Reflection (XRR). Thickness of BTO films was further confirmed by STEM measurements.

Device Fabrication

Top electrodes with radii of 5 μm, 10μm and 20μm on BTO/SNTO heterostructures were fabricated using ultraviolet lithography, thermal evaporation (Au, Cr and Ti) or e–beam evaporation (Pt). Capping layers of Au were adopted on Cr and Ti to prevent oxidation and followed by lift-off process. When not specifically indicated, the electrical properties of the BTO and STO based devices were measured with a top electrode radius of 5 μm.

Characterization

The BTO films crystal structures were characterized using STEM images. Cross-sectional HAADF images were recorded at 300 kV on the Titan Cubed Themis G2 300 aberration-corrected transmission electron microscope with the Gatan Enfinium^{TM}ER (Model 977) spectrometer. Using a home-made MatLab code, atom positions are determined by simultaneously fitting with 2D Gaussian peaks. The displacements of Ti columns respectively to the neighboring Ba is$\Delta_{total}=(\Delta_x^2+\Delta_y^2)^{1/2}$, where$\Delta_x$ and Δ_y are horizontal and vertical distance between Ti atom and the center of neighboring Ba atoms. Small systematic-error-displacements can exist in the bulk due to the tiny specimen mis-tilt between optical axis and specimen, which is unavoidable during experiments. The surface morphology, polarization imaging, local ferroelectric properties and current mapping were performed using a commercial scanning probe microscope (Asylum Research MFP3D). Pt/Ti-coated silicon cantilevers were adopted in the PFM images and conductive-diamond-coated silicon cantilevers were used in the C-AFM measurements. Local hysteretic behaviors of the PFM phase and amplitude signals were collected in DART (dual a.c. resonance tracking) mode and the signals were recorded while the voltage was off.

Electrical Measurement

Electrical measurements were performed by a Keithley 4200 semiconductor characterization system in a LakeShore TTPX cryogenic vacuum probe station with 3-μm tungsten probes. The test

pulses were applied to the metal electrodes and the SNTO substrates were grounded, where positive bias means currents flow from the metal electrodes to the SNTO substrates.

Supplemental References

Fan, Z., Fan, H., Yang, L., Li, P., Lu, Z., Tian, G., Huang, Z., Li, Z., Yao, J., Luo, Q. et al. (2017). Resistive switching induced by charge trapping/detrapping: a unified mechanism for colossal electroresistance in certain Nb:$SrTiO_3$-based heterojunctions. J. Mater. Chem. C *5*, 7317-7327.

Gruverman, A., Wu, D., Lu, H. Wang, Y. Jang, H. W., Folkman, C. M., Zhuravlev, M. Ye., Felker, D., Rzchowski, M., Eom, C.-B., and Tsymbal, E. Y. (2009). Tunneling Electroresistance Effect in ferroelectric Tunnel Junctions at the Nanoscale. Nano Lett. *9*, 3539-3543.

Jiang, L., Choi, W. S., Jeen, H., Dong, S., Kim, Y., Han, M. G., Zhu, Y., Kalinin, S. V., Dagotto, E., Egami, T., and Lee, H. N. (2013). Tunneling electroresistance induced by interfacial phase transitions in ultrathin oxide heterostructures. Nano Lett. *13*, 5837-5843.

Kim, D. J., Lu, H., Ryu, S., Bark, C.-W., Eom, C.-B., Tsymbal, E. Y., and Gruverman, A. (2012). Ferroelectric tunnel memristor. Nano Lett. *12*, 5697-5702.

Lu, H., Lipatov, A., Ryu, S., Kim, D. J., Lee, H., Zhuravlev, M. Y., Eom, C. B., Tsymbal, E. Y., Sinitskii, A., and Gruverman, A. (2014). Ferroelectric tunnel junctions with graphene electrodes. Nat. Commun. *5*, 5518.

Pantel, D., and Alexe, M. (2010). Electroresistance effects in ferroelectric tunnel barriers. Phys. Rev. B *82*, 134105.

Wang, L., Cho, M. R., Shin, Y. J., Kim, J. R., Das, S., Yoon, J.-G., Chung, J.-S., and Noh, T. W. (2016). Overcoming the Fundamental Barrier Thickness Limits of Ferroelectric Tunnel Junctions through $BaTiO_3$/$SrTiO_3$ Composite Barriers. Nano Lett. *16*, 3911-3918.